Constraints on multifield inflation from the BOSS galaxy survey

Giovanni Cabass,[1,*] Mikhail M. Ivanov,[1,†] Oliver H. E. Philcox,[2,1]
Marko Simonović,[3] and Matias Zaldarriaga[1]

[1]*School of Natural Sciences, Institute for Advanced Study,*
1 Einstein Drive, Princeton, New Jersey 08540, USA
[2]*Department of Astrophysical Sciences, Princeton University, Princeton, New Jersey 08540, USA*
[3]*Theoretical Physics Department, CERN, 1 Esplanade des Particules, Geneva 23, CH-1211, Switzerland*

We use redshift-space galaxy clustering data from the BOSS survey to constrain local primordial non-Gaussianity (LPNG). This is of particular importance due to the consistency relations, which imply that a detection of LPNG would rule out all single-field inflationary models. Our constraints are based on the consistently analyzed redshift-space galaxy power spectra and bispectra, extracted from the public BOSS data with optimal window-free estimators. We use a complete perturbation theory model including all one-loop power spectrum corrections generated by LPNG. Our constraint on the amplitude of the local non-Gaussian shape is $f_{\rm NL}^{\rm local} = -33 \pm 28$ at 68% C.L., yielding no evidence for primordial non-Gaussianity. The addition of the bispectrum tightens the $f_{\rm NL}^{\rm local}$ constraints from BOSS by 20%, and allows breaking of degeneracies with non-Gaussian galaxy bias. These results set the stage for the analysis of future surveys, whose larger volumes will yield significantly tighter constraints on LPNG.

I. INTRODUCTION

Inflation provides a mechanism to seed density fluctuations that we observe in the late Universe. The physics responsible for it, which may have operated at energies as high as 10^{16} GeV, has left observable imprints in these density fluctuations. The observations of cosmic microwave background (CMB) anisotropies and the distribution of galaxies in the large-scale structure (LSS) present particularly appealing ways to probe the inflationary epoch, and thus the physics of this high-energy regime.

There is a special class of inflationary models, in which inflation is driven by a medium whose quantum fluctuations are the only source of the observable overdensities. Assuming the attractor solution and the Bunch-Davies vacuum, these *single-field* (or single-clock) models generically predict purely adiabatic fluctuations with vanishing physical coupling of long-wavelength and short-wavelength modes. This result is formalized in the well-known consistency relations [1,2]. Given the bispectrum $B_\phi(k_1, k_2, k_3)$ of the primordial Bardeen potential ϕ, they have the following form

$$B_\phi(k_1, k_2, k_3)|_{k_3 \ll k_1, k_2} = -\frac{5}{3} P_\phi(k_3) \left[3 + k_1 \frac{\partial}{\partial k_1}\right] P_\phi(k_1). \quad (1)$$

This limit, when one of the wave numbers is much smaller than the other two, is called the squeezed limit. Equation (1) implies that in single-field models the only effect of the long-wavelength modes of ϕ on the short-scale modes is a simple rescaling of coordinates, which is locally unobservable. Therefore, any detection of local primordial non-Gaussianity (LPNG), i.e., a detection of a nonvanishing amplitude in the squeezed limit of the initial bispectrum due to physical interactions of long and short modes, would rule out single-field inflation [2].

While the simplicity of single-field inflation is very appealing (and so far supported by observations), having more than one relevant fluctuating degree of freedom besides the inflaton is easy to achieve. Some well-known examples are the curvaton scenario [3–5] and modulated reheating [6]. In contrast to single-field inflation, these *multifield* models can produce large and observable LPNG.

This important distinction between the two classes of inflationary models makes the amplitude of the initial bispectrum containing LPNG, called $f_{\rm NL}^{\rm local}$, the key observable that we can use to make quantitative, model-independent statements about the primordial Universe. It is defined in the following way

$$B_\phi(k_1, k_2, k_3) = 6 f_{\rm NL}^{\rm local} \Delta_\phi^4 \frac{\mathcal{S}_{\rm local}(k_1, k_2, k_3)}{k_1^2 k_2^2 k_3^2}, \quad (2)$$

*gcabass@ias.edu
†ivanov@ias.edu

where Δ_ϕ^2 is the amplitude of the primordial power spectrum $k^3 P_\phi(k) = \Delta_\phi^2 (k/k_*)^{n_s - 1}$ and n_s is the spectral index.[1] The local template is given by

$$\mathcal{S}_{\text{local}}(k_1, k_2, k_3) = \frac{1}{3}\frac{k_1^2}{k_2 k_3} + 2 \text{ perms.} \qquad (3)$$

This template is such that the squeezed limit bispectrum generated by the LPNG takes the following form

$$B_\phi(k_1, k_2, k_3)|_{k_3 \ll k_1, k_2} = 4 f_{\text{NL}}^{\text{local}} P_\phi(k_1) P_\phi(k_3), \qquad (4)$$

which is very different from the single-field result given by Eq. (1). Generic values of $f_{\text{NL}}^{\text{local}}$ in multifield models are of order one or higher (for some counterexamples, see [8,9]), making $f_{\text{NL}}^{\text{local}} \approx 1$ an interesting and well-motivated observational target.

Significant efforts are aimed at measuring $f_{\text{NL}}^{\text{local}}$, with the tightest current constraints coming from CMB observations. In particular, the *Planck* 2018 data yields $f_{\text{NL}}^{\text{local}} = -0.9 \pm 5.1$ [10]. Measurements from galaxy clustering are currently somewhat weaker, but are expected to improve significantly with upcoming galaxy surveys. These surveys will eventually reach the target of $f_{\text{NL}}^{\text{local}} \approx 1$ (see for example [11–13]). Almost all LSS analyses done so far use the fact that LPNG produces the so-called scale-dependent galaxy bias [14,15], and therefore can be constrained by observations of galaxy power spectra on large scales [16–20]. While measuring the galaxy power spectrum and looking for scale-dependent bias has the advantage of being relatively straightforward, this may not be an optimal way to constrain LPNG from LSS data. Indeed, as many Fisher forecasts and full likelihood analyses indicate, the dominant source of information on $f_{\text{NL}}^{\text{local}}$ for the shot-noise limited samples is the galaxy bispectrum [11,12,21–24]. Developing consistent and robust pipelines to harvest this information is one of the major milestones on the way toward achieving the tightest possible bounds on LPNG.

Performing an optimal search for LPNG in the observed galaxy bispectrum is not a trivial task for a number of reasons. One of the main difficulties is the survey geometry, which mixes the Fourier modes on large scales. In order to circumvent this problem, in this paper we use recently developed optimal window-free power spectrum and bispectrum estimators [25,26]. In principle, such an approach guarantees that the results are unbiased, close-to-optimal and that all effects related to the window function are consistently taken into account. This is particularly important for constraints on $f_{\text{NL}}^{\text{local}}$, since most of the signal comes from the largest scales in the survey, either through the

scale-dependent bias or through the squeezed triangles. An alternative is to model the effects of window convolution when calculating the observed bispectrum. Doing this exactly is very challenging numerically, and novel methods to tackle this problem were developed only very recently [27]. On the other hand, if the effects of the window function are modeled using approximate treatments available in the literature (e.g., [28,29]), this can lead to biases at low k, leading to such bins needing to be dropped from the analysis. This approach was used recently in [30] to measure LPNG, and it remains unclear to what extent the results are impacted by the approximate treatment of the window function.

Another nontrivial task is the modeling of the galaxy bispectrum signal. This includes all aspects of the nonlinear evolution such as the backreaction of short-scale physics on large-scale modes, the nonlinear evolution of the BAO signature (IR resummation), as well as a robust control over projection and binning effects. Many years of intense theoretical efforts [31–47] have recently made the incorporation of these effects possible, so that the bispectrum data can be routinely used in cosmological parameter analyses [48].

In this work, we present a search of LPNG using galaxy power spectrum and bispectrum from the publicly available BOSS data [49]. This is a natural continuation of our previous analysis of PNG in single-field inflation [50], based on the same tree-level bispectrum model and the data cuts that were extensively tested in [47]. Importantly, the galaxy bispectrum treatment presented in [47] is fully systematic, i.e., there is a way to control the precision of various effects so it can be applied to future high-precision galaxy survey data.

The remainder of this paper is structured as follows. In Sec. II we present key theoretical ingredients needed to extract LPNG from the galaxy clustering data. They include the complete calculation of the one-loop galaxy power spectrum in the presence of LPNG. Section III describes the data and analysis details. We validate our pipeline on the mock galaxy clustering data in Sec. IV, and then apply it to the BOSS data in Section V. We present limits on non-Gaussian bias parameters from the BOSS data in Sec. VI. Section VII draws conclusions. Additional details of the theory model are given in the Appendix A.

II. STRUCTURE FORMATION IN THE PRESENCE OF LPNG

In this section we present our theoretical model, which includes all necessary terms generated by LPNG. We work in the framework of the effective field theory of large scale structure (hereafter EFT of LSS), as described in [51–56] and references therein. Since the perturbative model for structure formation has been discussed in detail in the works cited above, we will provide only a brief overview in what follows, focusing on the ingredients that will be

---

[1] *Planck* 2018 [7] gives precise measurements for both of these quantities: $\Delta_\phi^2 \approx 1.5 \times 10^{-8}$ and $n_s \approx 0.96$, for the pivot scale $k_* = 0.05 \text{ Mpc}^{-1}$.

necessary to carry out the calculation of the one-loop LPNG contributions. For dark matter and biased tracers in real space, these contributions have already been studied in the literature, [23,57–59]. Here, we extend these results to the case of galaxies in redshift-space needed for comparison to observations.

To simplify the text and formulas, we omit the superscript "local" in our notation of the f_{NL} parameter in this section. We stress, however, that all results obtained here, strictly speaking, apply only to the case of LPNG. The analogous theory model for nonlocal primordial non-Gaussianity is presented in Ref. [50].

A. Gaussian part

For Gaussian initial conditions, the statistical properties of the first-order density field, $\delta^{(1)}$, are completely determined by its power spectrum P_{11}:

$$\langle \delta^{(1)}(\mathbf{k})\delta^{(1)}(\mathbf{k}')\rangle = (2\pi)^3 \delta_D^{(3)}(\mathbf{k}' + \mathbf{k})P_{11}(k), \quad (5)$$

where we have suppressed the explicit time dependence for brevity. In this work, we restrict our analysis of the galaxy power spectrum to one-loop order in the EFT of LSS, where the usual Gaussian part reads

$$P_{\text{Gauss}} = P_{\text{tree}} + P_{1-\text{loop}} + P_{\text{ctr}} + P_{\text{stoch}}, \quad (6)$$

where P_{tree} is the linear term, $P_{1-\text{loop}}$ is the one-loop correction (with Gaussian initial conditions), P_{ctr} is the higher derivative term (counterterm), and P_{stoch} is the term that captures galaxy stochasticity.

We now present our model for the galaxy bias, referring the interested reader to [42] for an extensive review. For the statistics considered herein, it is sufficient to consider the galaxy density field at cubic order. We use the following set of bias operators

$$\delta_g^{(r)} = b_1\delta + \frac{b_2}{2}\delta^2 + b_{\mathcal{G}_2}\mathcal{G}_2 + \frac{b_3}{6}\delta^3 + b_{\delta\mathcal{G}_2}\delta\mathcal{G}_2 + b_{\mathcal{G}_3}\mathcal{G}_3$$
$$+ b_{\Gamma_3}\Gamma_3 + R_*^2\partial^2\delta. \quad (7)$$

The Galileon operator $\mathcal{G}_2$ is defined as $(\partial_i\partial_j\Phi_g)^2 - (\partial^2\Phi_g)^2$, where Φ_g is the gravitational potential. The Γ_3 operator instead is defined as $\mathcal{G}_2[\Phi_g] - \mathcal{G}_2[\Phi_v]$, where Φ_v is the velocity potential. The cubic operators δ^3, $\delta\mathcal{G}_2$, $\mathcal{G}_3$ do not contribute to the one-loop power spectrum after renormalization.

The redshift-space mapping for fixed line of sight $\hat{\mathbf{z}}$ at order $(\delta^{(1)})^3$ is given by

$$\delta_g^{(s)} = \delta_g^{(r)} - \partial_z(u_z(1+\delta_g^{(r)})) + \frac{1}{2}\partial_z^2(u_z^2(1+\delta_g^{(r)})) - \frac{1}{6}\partial_z^3(u_z^3), \quad (8)$$

(from expanding the usual real-space to redshift-space relation), where $u_z \equiv \hat{\mathbf{z}} \cdot \mathbf{v}/\mathcal{H}$, $\mathbf{v}$ is the peculiar velocity field and $\mathcal{H}$ is the conformal Hubble parameter. These can be written in terms of the Fourier-space kernels

$$Z_1(\mathbf{k}) = b_1 + f\mu^2,$$

$$Z_2(\mathbf{k}_1, \mathbf{k}_2) = \frac{b_2}{2} + b_{\mathcal{G}_2}\left(\frac{(\mathbf{k}_1 \cdot \mathbf{k}_2)^2}{k_1^2 k_2^2} - 1\right)$$
$$+ b_1 F_2(\mathbf{k}_1, \mathbf{k}_2) + f\mu^2 G_2(\mathbf{k}_1, \mathbf{k}_2)$$
$$+ \frac{f\mu k_{12}}{2}\left(\frac{\mu_1}{k_1}(b_1 + f\mu_2^2) + \frac{\mu_2}{k_2}(b_1 + f\mu_1^2)\right), \quad (9)$$

and Z_3, whose expression can be found in Sec. 2 of [60], where f is the logarithmic growth rate and $\mu = \hat{\mathbf{k}} \cdot \hat{\mathbf{z}}$. In this notation, the deterministic part of the redshift-space galaxy density field can be written as

$$\delta_g(\mathbf{k}) = Z_1(\mathbf{k})\delta^{(1)}(\mathbf{k}) + \int_{\mathbf{p}_{12}=\mathbf{k}} Z_2(\mathbf{p}_1, \mathbf{p}_2)\delta^{(1)}(\mathbf{p}_1)\delta^{(1)}(\mathbf{p}_2)$$
$$+ \int_{\mathbf{p}_{123}=\mathbf{k}} Z_3(\mathbf{p}_1, \mathbf{p}_2, \mathbf{p}_3)\delta^{(1)}(\mathbf{p}_1)\delta^{(1)}(\mathbf{p}_2)\delta^{(1)}(\mathbf{p}_3), \quad (10)$$

where we have introduced the following notation $\int_{\mathbf{p}_{1...n}=\mathbf{k}} \equiv \int \frac{d^3\mathbf{p}_1}{(2\pi)^3}\cdots\frac{d^3\mathbf{p}_n}{(2\pi)^3}(2\pi)^3\delta^D(\mathbf{k} - \mathbf{p}_{1...n})$ and $\mathbf{p}_{1...n} \equiv \mathbf{p}_1 + \cdots + \mathbf{p}_n$. We also supplement these kernels with the appropriate redshift-space counterterms that are omitted in (8) for clarity; these are discussed in Ref. [47].

B. LPNG-related nonlinearity

LPNG affects the statistics of the galaxy overdensity in two ways. First, we have a nonzero bispectrum for the linear matter overdensity $\delta^{(1)}$. This generates a connected bispectrum contribution B_{111},

$$\langle \delta^{(1)}(\mathbf{k}_1)\delta^{(1)}(\mathbf{k}_2)\delta^{(1)}(\mathbf{k}_3)\rangle$$
$$\equiv (2\pi)^3\delta_D^{(3)}(\mathbf{k}_{123})B_{111}(k_1, k_2, k_3)$$
$$= (2\pi)^3\delta_D^{(3)}(\mathbf{k}_{123})\prod_{a=1}^{3}\mathcal{M}(k_a)B_\phi(k_1, k_2, k_3), \quad (11)$$

where we have introduced the transfer functions

$$\delta^{(1)}(\mathbf{k}) = \mathcal{M}(k)\phi(\mathbf{k}) \Rightarrow \mathcal{M}(k) = \sqrt{\frac{P_{11}(k)}{P_\phi(k)}}. \quad (12)$$

The initial bispectrum (11) also generates an additional loop correction to the matter power spectrum dubbed P_{12}. We will discuss this term shortly.

Second, LPNG modulates the correlation between the long and short modes, which ultimately alters the probability of galaxy formation (inducing scale-dependent bias [14,15]). In order to reproduce this effect in the perturbative galaxy bias expansion, one needs to include new operators with the appropriate bias coefficients analogous to the Gaussian case (7). At linear order in $f_{NL}\Delta_\phi$ and cubic order in $\delta^{(1)}$ these operators are given by

$$\delta_g^{LPNG}(\mathbf{x}) = b_\phi f_{NL}\phi(\mathbf{q}) + b_{\phi\delta}f_{NL}\phi(\mathbf{q})\delta(\mathbf{x})$$
$$+ b_{\phi\delta^2}f_{NL}\phi(\mathbf{q})\delta^2(\mathbf{x}) + b_{\phi\mathcal{G}_2}f_{NL}\phi(\mathbf{q})\mathcal{G}_2(\mathbf{x}). \quad (13)$$

Note that this expansion is valid only for LPNG. For nonlocal primordial non-Gaussianity the squeezed bispectrum is typically proportional to derivatives of ϕ, and hence ϕ in the above expansion must be replaced by appropriate higher derivative operators like $\partial^2\phi$ [61]. These operators appear to be higher order and hence their effect can be neglected at the one-loop order in the EFT of LSS [50].

In contrast to Eq. (7), here we have made the argument of all relevant fields explicit. More precisely, the Bardeen potential appearing on the right-hand side is evaluated at the Lagrangian position $\mathbf{q}$ corresponding to the Eulerian position $\mathbf{x}$ [23,58,59]. In order to evaluate all fields at the Eulerian coordinates we need to Taylor expand the primordial gravitational potential. If we want to keep all terms up to cubic order we can write

$$\phi(\mathbf{q}) = \phi(\mathbf{x} - \boldsymbol{\psi}(\mathbf{q})) = \phi(\mathbf{x} - \boldsymbol{\psi}(\mathbf{x} - \boldsymbol{\psi}(\mathbf{x}))). \quad (14)$$

Expanding perturbatively in the displacement field $\boldsymbol{\psi}$ we get

$$\phi(\mathbf{q}) = \phi - \psi^i\partial_i\phi + \psi^k(\partial_k\psi^i)\partial_i\phi + \frac{1}{2}\psi^i\psi^j\partial_i\partial_j\phi, \quad (15)$$

where the fields on the right-hand side are all evaluated at the Eulerian position $\mathbf{x}$, and we emphasize that the displacement ψ contains both the linear and the second-order contribution. We keep terms up to cubic order in the expansion (15) since they are needed for the consistent

calculation of the one-loop power spectrum. Before we move on, let us comment on the omission of higher derivative terms of the form $\partial_\mathbf{q}^2\phi(\mathbf{q})$ in (13). These corrections can be straightforwardly included, see e.g., [58], but for realistic values of f_{NL} they are always suppressed compared to the two-loop Gaussian contributions that we neglect here. Therefore, we neglect the higher derivative LPNG terms in what follows.

Let us now shift our attention to redshift-space. In this case LPNG generates additional counterterms in δ_g involving the matter velocity field $\mathbf{v}$. However, as we have just discussed, these terms can be neglected in our analysis because they have the same order of magnitude as the higher derivative LPNG operators. Hence, it is enough to use (8) to map the rest-frame galaxy overdensity in presence of LPNG to redshift-space.

All in all, the Taylor expansion of δ_{NL} though $\delta^{(1)}$ in the presence of LPNG will take a form identical to Eq. (10), but with the new kernels $Z_n^{tot} = Z_n + Z_n^{NG}$ ($n = 1, 2, 3$), where Z_n^{NG} are the additional PNG kernel contributions. The linear kernel is given by

$$Z_1^{NG}(k) = b_\phi f_{NL}, \quad (16)$$

with the second kernel taking the form

$$Z_2^{NG}(\mathbf{p}_1, \mathbf{p}_2) = b_\phi f_{NL}\frac{\mathbf{p}_1 \cdot \mathbf{p}_2}{2p_1 p_2}\left(\frac{p_2}{p_1}\frac{1}{\mathcal{M}(p_2)} + \frac{p_1}{p_2}\frac{1}{\mathcal{M}(p_1)}\right)$$
$$+ b_\phi f_{NL}\frac{f\mu k}{2}\left(\frac{\mu_1}{p_1}\frac{1}{\mathcal{M}(p_2)} + \frac{\mu_2}{p_2}\frac{1}{\mathcal{M}(p_1)}\right)$$
$$+ b_{\phi\delta}f_{NL}\frac{1}{2}\left(\frac{1}{\mathcal{M}(p_1)} + \frac{1}{\mathcal{M}(p_2)}\right), \quad (17)$$

where we have introduced

$$\mu_i = \hat{\mathbf{z}} \cdot \hat{\mathbf{p}}_i, \qquad \mu_{ij} = \hat{\mathbf{z}} \cdot (\mathbf{p}_i + \mathbf{p}_j)/|\mathbf{p}_i + \mathbf{p}_j|. \quad (18)$$

For the cubic fields we find

$$Z_3^{NG}(\mathbf{p}_1, \mathbf{p}_2, \mathbf{p}_3) = b_\phi f_{NL}\left(-\frac{1}{14}\mathcal{G}_2(\mathbf{p}_1, \mathbf{p}_2)\frac{(\mathbf{p}_1 + \mathbf{p}_2) \cdot \mathbf{p}_3}{|\mathbf{p}_1 + \mathbf{p}_2|^2}\frac{1}{\mathcal{M}(p_3)} + 2\text{ perms}\right) + b_\phi f_{NL}\left(\frac{1}{6}\frac{\mathbf{p}_1 \cdot \mathbf{p}_2}{p_1^2 p_2^2}\frac{\mathbf{p}_2 \cdot \mathbf{p}_3}{\mathcal{M}(p_3)} + 5\text{ perms}\right)$$
$$+ b_\phi f_{NL}\left(\frac{1}{6}\frac{\mathbf{p}_1 \cdot \mathbf{p}_3}{p_1^2 p_2^2}\frac{\mathbf{p}_2 \cdot \mathbf{p}_3}{\mathcal{M}(p_3)} + 2\text{ perms}\right) + b_\phi f_{NL}f\mu p_{123}\left(\frac{1}{3}G_2(\mathbf{p}_1, \mathbf{p}_2)\frac{\mu_{12}}{|\mathbf{p}_1 + \mathbf{p}_2|}\frac{1}{\mathcal{M}(p_3)} + 2\text{ perms}\right)$$
$$+ b_\phi f_{NL}(f\mu p_{123})^2\left(\frac{1}{6}\frac{\mu_1\mu_2}{p_1 p_2}\frac{1}{\mathcal{M}(p_3)} + 2\text{ perms}\right). \quad (19)$$

Note that $b_{\phi\delta^2}$ and $b_{\phi\mathcal{G}_2}$ do not appear in Z_3^{NG}: the reason for this is that they are removed after renormalization of b_1 and b_ϕ. Moreover, the contributions from $b_{\phi\delta}$ where either ϕ or δ are expanded at second order in perturbations are also

absorbed by renormalization of these two parameters, was first proved in Ref. [23] in the context of the real space perturbation theory. Finally, let us note that compared to the analysis of [30], we include the cubic non-Gaussian kernel

in the model, which is needed to calculate corrections to the one-loop galaxy power spectrum induced by LPNG.

C. Stochasticity

So far we have focused on the deterministic part of the galaxy overdensity. PNG leads to additional contributions to the stochastic part of δ_g as we discuss below.

References [42,47,52] contain a detailed description of stochastic terms in the case of Gaussian initial conditions. As far as the tree-level bispectrum and one-loop power spectrum in the presence of LPNG are concerned, the full stochastic contribution is given by [47,51]

$$
\begin{aligned}
\delta_g^{\text{stoch}}(\mathbf{k}) &= \epsilon + \frac{d_2}{2} b_1 [\delta\epsilon]_{\mathbf{k}} - f[\partial_z(\epsilon u_z)]_{\mathbf{k}} + f_{\text{NL}} \frac{b_{\epsilon\phi}}{2} [\epsilon\phi]_{\mathbf{k}} \\
&\quad + a_0 R_*^2 k^2 \epsilon + a_2 k_z \hat{z}^i (\epsilon^i + k^i \epsilon) + a_4 k_z^2 \hat{z}_i \hat{z}_j \epsilon^{ij},
\end{aligned}
\tag{20}
$$

where $\epsilon, \epsilon^i, \epsilon^{ij}$ are the stochastic density, velocity and tidal fields. The final three terms in (20) are higher derivative stochastic contributions that are important only for the Gaussian part. The only new LPNG contribution here is $\epsilon\phi$, where we emphasize again that ϕ is evaluated at the Lagrangian position $\mathbf{q}$.

D. Summary of the power spectrum and bispectrum models

Once the new kernels in the presence of LPNG are obtained, it is straightforward to compute the one-loop power spectrum and the tree-level bispectrum. Modulo the counterterms, the deterministic part is given by

$$
\begin{aligned}
P_{\text{1-loop}}^{\text{tot}} &= 2 \int_{\mathbf{p}} [Z_2^{\text{tot}}(\mathbf{p}, \mathbf{k} - \mathbf{p})]^2 P_{11}(p) P_{11}(|\mathbf{k} - \mathbf{p}|) \\
&\quad + 6 Z_1^{\text{tot}}(\mathbf{k}) P_{11}(k) \int_{\mathbf{p}} Z_3^{\text{tot}}(\mathbf{k}, -\mathbf{p}, \mathbf{p}) P_{11}(p) \\
&\quad + 2 Z_1^{\text{tot}}(\mathbf{k}) \int_{\mathbf{p}} Z_2^{\text{tot}}(\mathbf{p}, \mathbf{k} - \mathbf{p}) B_{111}(k, p, |\mathbf{k} - \mathbf{p}|), \\
B_{\text{tree}}^{\text{tot}} &= Z_1^{\text{tot}}(\mathbf{k}_1) Z_1^{\text{tot}}(\mathbf{k}_2) Z_1^{\text{tot}}(\mathbf{k}_3) B_{111}(k_1, k_2, k_3) \\
&\quad + 2 Z_2^{\text{tot}}(\mathbf{k}_1, \mathbf{k}_2) Z_1^{\text{tot}}(\mathbf{k}_1) Z_2^{\text{tot}}(\mathbf{k}_2) P_{11}(k_1) P_{11}(k_2) \\
&\quad + \text{perms.}
\end{aligned}
\tag{21}
$$

It is instructive to simplify this expression and break it down into separate pieces. In this section we give explicit expressions for different terms in Eq. (21). We focus on contributions that are linear in $f_{\text{NL}}^{\text{local}} \Delta_\phi$. The contributions $\mathcal{O}((f_{\text{NL}}^{\text{local}} \Delta_\phi)^2)$ can be straightforwardly computed, but turn out to be irrelevant for our analysis (as shown in Sec. II E) except for the linear f_{NL}^2 scale-dependent bias term. We briefly discuss other $\mathcal{O}((f_{\text{NL}}^{\text{local}} \Delta_\phi)^2)$ corrections in Appendix A.

1. Power spectrum

The power spectrum has three kinds of additional contributions proportional to f_{NL}. At tree level we have

$$
P_{\text{tree-level}}^{\text{LPNG}} = P_{11}^{f_{\text{NL}}} + P_{11}^{f_{\text{NL}}^2},
\tag{22}
$$

while at one-loop order the total contribution linear in $f_{\text{NL}}^{\text{local}}$ is given by

$$
P_{\text{1-loop}}^{\text{LPNG}} = P_{22}^{f_{\text{NL}}} + P_{13}^{f_{\text{NL}}} + P_{12}.
\tag{23}
$$

The first contributions are the scale-dependent bias

$$
\begin{aligned}
P_{11}^{f_{\text{NL}}}(k, \mu) &= 2(b_1 + f\mu^2) b_\phi f_{\text{NL}} \frac{P_{11}(k)}{\mathcal{M}(k)}, \\
P_{11}^{f_{\text{NL}}^2}(k, \mu) &= b_\phi^2 f_{\text{NL}}^2 \frac{P_{11}(k)}{\mathcal{M}^2(k)}.
\end{aligned}
\tag{24}
$$

Defining $P_{1\phi}(k) \equiv P_{11}(k)/\mathcal{M}(k)$, the $P_{22}^{f_{\text{NL}}}$ contribution can be written as

$$
\begin{aligned}
P_{22}^{f_{\text{NL}}}(\mathbf{k}) &= 4 f_{\text{NL}} \int_{\mathbf{p}} \tilde{Z}_2^{\text{NG}}(\mathbf{p}, \mathbf{k} - \mathbf{p}) Z_2(\mathbf{p}, \mathbf{k} - \mathbf{p}) P_{11}(p) \\
&\quad \times P_{1\phi}(|\mathbf{k} - \mathbf{p}|),
\end{aligned}
\tag{25}
$$

where we have introduced the new kernel

$$
\tilde{Z}_2^{\text{NG}}(\mathbf{p}_1, \mathbf{p}_2) = b_\phi \frac{\mathbf{p}_1 \cdot \mathbf{p}_2}{p_1^2} + b_\phi f \mu k \frac{\mu_1}{p_1} + b_{\phi\delta},
\tag{26}
$$

which is just a simplified version of Z_2^{NG}. The use of $P_{1\phi}$ and $\tilde{Z}_2^{\text{NG}}$ is particularly convenient for the FFTLog evaluation of $P_{22}^{f_{\text{NL}}}$, which we perform in this work following the approach of [62]. $P_{13}^{f_{\text{NL}}}$ is given by the sum of three contributions:

$$
P_{13}^{f_{\text{NL}}} = P_{13}^{f_{\text{NL}}(1)} + P_{13}^{f_{\text{NL}}(2)} + P_{13}^{f_{\text{NL}}(3)}.
\tag{27}
$$

The first is simply

$$
P_{13}^{f_{\text{NL}}(1)} = \frac{b_\phi f_{\text{NL}}}{\mathcal{M}(k)} \int_{\mathbf{p}} 6 Z_3(\mathbf{k}, \mathbf{p}, -\mathbf{p}) P_{11}(p),
\tag{28}
$$

with the second being

$$
P_{13}^{f_{\text{NL}}(2)} = -Z_1(\mathbf{k}) b_\phi f_{\text{NL}} k^2 (1 + f^2 \mu^2) \sigma_v^2 P_{1\phi}(k),
\tag{29}
$$

where $\sigma_v^2 \equiv \int_0^\infty \mathrm{d}q P_{11}(q)/6\pi^2$. This comes from the terms $\psi^i \psi^j \partial_i \partial_j \phi/2$ in (15) and $\partial_z^2(u_z^2 \phi)/2$ in the redshift-space mapping of $b_\phi f_{\text{NL}} \phi$, i.e., the third and fifth terms in (19). The contribution $P_{13}^{f_{\text{NL}}(2)}$ exactly cancels with the IR limit of the $P_{22}^{f_{\text{NL}}}$ integral just like the IR limits of the P_{13} and P_{22}

contributions in the Gaussian case. Finally, there is a term of the form

$$P_{13}^{f_{NL}(3)} = Z_1(\mathbf{k})P_{11}(k)\int_{\mathbf{p}} 6\tilde{Z}_3^{NG}(\mathbf{k},\mathbf{p},-\mathbf{p})P_{11}(p), \quad (30)$$

where

$$\tilde{Z}_3^{NG}(\mathbf{p}_1,\mathbf{p}_2,\mathbf{p}_3)$$
$$= b_\phi f_{NL}\left(-\frac{1}{14}\mathcal{G}_2(p_1,p_2)\frac{(p_1+p_2)\cdot p_3}{|p_1+p_2|^2}\frac{1}{\mathcal{M}(p_3)}+2\,\text{perms}\right)$$
$$+ b_\phi f_{NL}\left(\frac{1}{6}\frac{p_1\cdot p_2}{p_1^2 p_2^2}\frac{p_2\cdot p_3}{\mathcal{M}(p_3)}+5\,\text{perms}\right)$$
$$+ b_\phi f_{NL}f\mu p_{123}\left(\frac{1}{3}G_2(\mathbf{p}_1,\mathbf{p}_2)\frac{\mu_{12}}{|\mathbf{p}_1+\mathbf{p}_2|}\frac{1}{\mathcal{M}(p_3)}+2\,\text{perms}\right).$$
$$(31)$$

Notice that the only permutations surviving are those for which the transfer function remains inside the loop integral, i.e., it is $P_{1\phi}$ that is integrated in $P_{13}^{f_{NL}(3)}$. The last term P_{12} is given by

$$P_{12}(\mathbf{k}) = 12f_{NL}Z_1(\mathbf{k})\Delta_\phi\mathcal{T}(k)$$
$$\times \int_{\mathbf{p}}[\mathcal{S}(k,p,|\mathbf{k}-\mathbf{p}|)Z_2(\mathbf{p},\mathbf{k}-\mathbf{p})]$$
$$\times \mathcal{T}(p)\mathcal{T}(|\mathbf{k}-\mathbf{p}|), \quad (32)$$

where we have defined $\mathcal{T}(k) \equiv \Delta_\phi\mathcal{M}(k)/k^2$.

Finally, we note that the contribution from the stochastic term $\epsilon\phi$ to the one-loop power spectrum is degenerate with the stochastic shot noise contributions we have in the zero-f_{NL} case. For this reason we do not include it in the model.

The Gaussian and non-Gaussian one-loop corrections to the galaxy power spectrum monopole are shown in the left and right panels of Fig. 1, respectively, for $f_{NL} = 100$. We show all separate shapes without multiplying them by the nuisance parameters to clearly illustrate the size of these terms regardless of particular galaxy samples. The terms labeled "no biases" correspond to pure matter contributions (i.e., they have $b_1 = 1$ and all other biases set to zero, which corresponds a contribution from pure matter). We see that some of the LPNG loops are actually as large as the matter loops for $k \lesssim 0.1\ h\text{Mpc}^{-1}$. Thus, these terms must be included for consistency.

2. Bispectrum

Working at tree level in perturbations and at the linear order in $f_{NL}\Delta_\phi$, the PNG contributions to the redshift-space bispectrum are

$$B_{\text{tree-level}}^{NG} = f_{NL}B_{211}^{f_{NL}} + B_{111}^{(s)}. \quad (33)$$

$B_{211}^{f_{NL}}$ arises from scale-dependent bias and is given by

$$B_{211}^{f_{NL}}(\mathbf{k}_1,\mathbf{k}_2,\mathbf{k}_3) = Z_1(\mathbf{k}_1)Z_1(\mathbf{k}_2)b_{\delta\phi}[P_{11}(k_1)P_{1\phi}(k_2)+P_{11}(k_2)P_{1\phi}(k_1)]$$
$$+ Z_1(\mathbf{k}_1)Z_1(\mathbf{k}_2)b_\phi\frac{\mathbf{k}_1\cdot\mathbf{k}_2}{k_1 k_2}\left(\frac{k_2}{k_1}\frac{1}{\mathcal{M}(k_2)}+\frac{k_1}{k_2}\frac{1}{\mathcal{M}(k_1)}\right)P_{11}(k_1)P_{11}(k_2)$$
$$+ Z_1(\mathbf{k}_1)Z_1(\mathbf{k}_2)b_\phi f\mu_{12}k_{12}\left(\frac{\mu_1}{k_1}\frac{1}{\mathcal{M}(k_2)}+\frac{\mu_2}{k_2}\frac{1}{\mathcal{M}(k_1)}\right)P_{11}(k_1)P_{11}(k_2)$$
$$+ 2b_\phi Z_2(\mathbf{k}_1,\mathbf{k}_2)[Z_1(\mathbf{k}_1)P_{11}(k_1)P_{1\phi}(k_2)+Z_1(\mathbf{k}_2)P_{11}(k_2)P_{1\phi}(k_1)] + 2\text{ permutations.} \quad (34)$$

$B_{111}^{(s)}$ is the standard tree-level redshift-space PNG contribution,

$$B_{111}^{(s)}(\mathbf{k}_1,\mathbf{k}_2,\mathbf{k}_3) = \prod_{a=1}^{3} Z_1(\mathbf{k}_a)\mathcal{M}(k_a)B_\phi(k_1,k_2,k_3)$$
$$= Z_1(\mathbf{k}_1)Z_1(\mathbf{k}_2)Z_1(\mathbf{k}_3)$$
$$\times f_{NL}\Delta_\phi 6\mathcal{S}(k_1,k_2,k_3)$$
$$\times \mathcal{T}(k_1)\mathcal{T}(k_1)\mathcal{T}(k_1). \quad (35)$$

So far we have discussed the deterministic contributions. In contrast to the power spectrum case, there is an additional

stochastic contribution that is not degenerate with the ones present also in the zero-f_{NL} case. This contribution comes from (20), and takes the form

$$B_{\text{stoch}}^{f_{NL}} = f_{NL}b_\phi\mathcal{M}^{-1}(k_1)Z_1(\mathbf{k}_1)P_{11}(k_1)P_\epsilon(k_2)$$
$$+ f_{NL}b_{\epsilon\phi}\mathcal{M}^{-1}(k_1)Z_1(\mathbf{k}_1)P_{11}(k_1)P_\epsilon(k_2)$$
$$+ 5\text{ perms}, \quad (36)$$

where $P_\epsilon(k)$ is the power spectrum of ϵ. At leading order it is proportional to the constant shot noise value $\bar{n}^{-1}$. As we
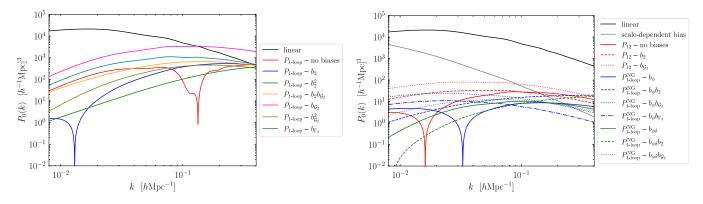
FIG. 1.   Left panel: "Gaussian" one-loop contributions to the power spectrum monopole at $z = 0.61$ compared with linear theory. We take $b_1 = 1$, and the different curves have the corresponding bias parameters set to unity. Right panel: PNG contributions to the power spectrum monopole at $z = 0.61$ compared with linear theory. We take $f_{\mathrm{NL}} = 100$ and $b_1 = 1$. The gray curve shows the scale-dependent bias contribution for $b_\phi = 1$. The remaining curves show the different contributions (P_{12} and $P_{22}^{f_{\mathrm{NL}}} + P_{13}^{f_{\mathrm{NL}}}$) to $P_{1\text{-loop}}^{\mathrm{NG}}$ for unit values of the corresponding bias parameters.

will argue shortly, these terms turn out to be irrelevant for our analysis.

Before closing this section, we also note that we have implemented IR resummation for all the LPNG terms entering the power spectra and bispectra models, following the formalism of time-sliced perturbation theory [38,44,63,64]. After implementing both IR resummation and the Alcock-Pazcynski projection effects [65] in our models for the tree-level bispectrum and the one-loop power spectra, we numerically compute the Legendre multipoles of the power spectrum and the bispectrum monopole, allowing for robust comparison to data.

E. Behavior in a scaling universe

Let us estimate the relative importance of the different f_{NL} contributions. This can be done using the scaling universe approach [58,66]. It is based on the fact that the linear power spectrum in our Universe can be well approximated by a power law: $P_{11} \propto (k/k_{\mathrm{NL}})^n k_{\mathrm{NL}}^{-3}$ with $n \approx -1.5$ for quasilinear wave numbers $k \simeq 0.1\ h\mathrm{Mpc}^{-1}$. We also introduced the nonlinear scale $k_{\mathrm{NL}} = 0.5\ h\mathrm{Mpc}^{-1}$ at $z = 0.5$.

We choose to focus on this particular range for the following reason. Given that the leading LPNG contribution is a linear scale-dependent bias enhanced on large scales, and the LPNG loop corrections dominate the usual Gaussian loops at low-k, large scales should be crucial for our analysis. The relative contributions of these terms diminish compared to the Gaussian loops at small scales, but the error bars also get smaller. This suggests that the relative importance of the LPNG corrections should be maximal at some intermediate wave number scale, which we choose we to be $k_{\mathrm{ref}} = 0.1\ h\mathrm{Mpc}^{-1}$, roughly in the center of the wave number range that we use in the data analysis. In what follows, all estimates will be presented for $k = k_{\mathrm{ref}}$.

Assuming that there is a single nonlinear scale in the problem, the estimates for the total dimensionless galaxy power spectrum $\Delta^2(k) \equiv k^3 P(k)$ for purely Gaussian initial conditions give

$$\Delta^2(k) = \underbrace{\left(\frac{k}{k_{\mathrm{NL}}}\right)^{1.5}}_{P_{\mathrm{tree}}} + \underbrace{\left(\frac{k}{k_{\mathrm{NL}}}\right)^{3}}_{P_{1\text{-loop}}} + \underbrace{\left(\frac{k}{k_{\mathrm{NL}}}\right)^{3.5}}_{\mathrm{ctr}} + \underbrace{\left(\frac{k}{k_{\mathrm{NL}}}\right)^{3}}_{\mathrm{stoch}}. \quad (37)$$

Recalling that the Bardeen potential has a nearly scale-invariant spectrum, we get the following expressions for the LPNG terms:

$$\Delta_{\mathrm{NG}}^2(k) = \underbrace{f_{\mathrm{NL}}\Delta_\phi\left(\frac{k}{k_{\mathrm{NL}}}\right)^{0.75}}_{P_{\mathrm{tree\text{-}level}}^{\mathrm{NG},f_{\mathrm{NL}}}} + \underbrace{(f_{\mathrm{NL}}\Delta_\phi)^2}_{P_{\mathrm{tree\text{-}level}}^{\mathrm{NG},f_{\mathrm{NL}}^2}}$$
$$+ \underbrace{f_{\mathrm{NL}}\Delta_\phi\left(\frac{k}{k_{\mathrm{NL}}}\right)^{2.25}}_{P_{1\text{-loop}}^{\mathrm{NG}}}. \quad (38)$$

Evaluating these corrections at the reference scale $k_{\mathrm{ref}} = 0.1\ h\mathrm{Mpc}^{-1}$, we get

$$\Delta_{P_{\mathrm{tree}}}^2 \simeq 0.089, \quad \Delta_{P_{1\text{-loop}}}^2 = \Delta_{P_{\mathrm{stoch}}}^2 \simeq 8 \times 10^{-3},$$

$$\Delta_{P_{\mathrm{ctr}}}^2 \simeq 3.6 \times 10^{-3}, \quad \Delta_{P_{\mathrm{tree\text{-}level}}^{\mathrm{NG},f_{\mathrm{NL}}}}^2 \simeq 1.1 \times 10^{-2} \times \frac{f_{\mathrm{NL}}}{300},$$

$$\Delta_{P_{\mathrm{tree\text{-}level}}^{\mathrm{NG},f_{\mathrm{NL}}^2}}^2 \simeq 1.3 \times 10^{-3} \times \left(\frac{f_{\mathrm{NL}}}{300}\right)^2, \quad \Delta_{P_{1\text{-loop}}^{\mathrm{NG}}}^2 \simeq 9.6 \times 10^{-4} \times \frac{f_{\mathrm{NL}}}{300}.$$
$$(39)$$

As expected, we see that the scale-dependent bias contribution $P_{\mathrm{tree\text{-}level}}^{\mathrm{LPNG}}$ always dominates over $P_{1\text{-loop}}^{\mathrm{LPNG}}$, and it is

the main source of constraining power in the power spectrum data. For $f_{\mathrm{NL}} \lesssim 300$ typical for our analyses we also see that the one-loop PNG contributions are a small fraction of the "Gaussian" $P_{\text{1-loop}}$.

The leading correction to the above result is given by the Gaussian two-loop contribution, which can be estimates as

$$\Delta^2_{\text{2-loop}} = \left(\frac{k_{\text{ref}}}{k_{\text{NL}}}\right)^{4.5} \simeq 7.2 \times 10^{-4}. \qquad (40)$$

This can be contrasted with the terms that we have dropped. Higher derivative f_{NL} contributions stemming down from terms like $\partial^2 \phi$ would be suppressed compared to other 1-loop LPNG terms that we retain in the theory model,

$$\Delta^2_{\langle \partial^2 \phi \delta \rangle} = f_{\mathrm{NL}} \Delta_\phi \left(\frac{k_{\text{ref}}}{k_{\text{NL}}}\right)^{2.75} \simeq 4.3 \times 10^{-4} \times \left(\frac{f_{\mathrm{NL}}}{300}\right). \quad (41)$$

This justifies our choice of dropping these terms in Sec. II B.

We can make a similar argument for the loop terms $\mathcal{O}(f^2_{\mathrm{NL}})$, which are also suppressed,

$$\Delta^2_{\langle \phi \delta^2 \rangle} = (f_{\mathrm{NL}} \Delta_\phi)^2 \left(\frac{k_{\text{ref}}}{k_{\text{NL}}}\right)^{1.5} \simeq 1.1 \times 10^{-4} \times \left(\frac{f_{\mathrm{NL}}}{300}\right)^2. \quad (42)$$

All in all, our scaling universe estimates confirm that the one-loop LPNG corrections can be important in the data analysis [23]. In addition, we also need to retain the leading f^2_{NL} tree-level power spectrum contribution.

For the squeezed-limit tree-level bispectrum, where the shape of LPNG plays the most important role, it is straightforward to see that $B^{f_{\mathrm{NL}}}_{211}$ and B_{111} scale in the same way. Their relative importance with respect to the "Gaussian" $B^{(s)}_{211}$ is the same as that of the scale-dependent bias piece versus P_{11} in the power spectrum. The contribution from $B^{f_{\mathrm{NL}}}_{\text{stoch}}$ is suppressed in the squeezed limit, and thus we do not include it in the analysis.

F. LPNG bias parameters

In the context of the EFT of LSS, b_ϕ and $b_{\phi\delta}$ (as well as usual bias parameters like b_1, b_2, etc.) should be treated as free nuisance parameters and marginalized over in data analysis. However, there are certain phenomenological models of dark matter halo formation, which predict b_ϕ and $b_{\phi\delta}$ parameters as a function of the linear bias b_1. These are known as "universality relations" [42]. For the relevant LPNG bias coefficients they predict

$$b_\phi = 2\delta_c(b_1 - 1),$$
$$b_{\phi\delta} = b_\phi - (b_1 - 1) + \delta_c\left[b_2 - \frac{8}{21}(b_1 - 1)\right], \qquad (43)$$

where $\delta_c = 1.686$. A typical approach then is to assume that the same relationship holds true even for galaxies. The universality relation is routinely used in most of f_{NL} constraints from galaxy surveys. However, the relationships (43) fail for galaxies [67] from realistic hydrodynamical simulations. The most accurate analysis to date gives the following fits based on the state-of-the art galaxy formation simulations [24,68]:

$$b_\phi = 2\delta_c(b_1 - 0.55),$$
$$b_{\delta\phi} = 3.85 - 9.49b_1 + 3.44b_1^2. \qquad (44)$$

We adopt relationship (44) in our baseline analysis. As a cross check, we also repeat our analysis for the vanilla universality relations (43). In Section VI we go beyond any assumptions on the LPNG parameters and fit $b_{\delta\phi} f^{\text{local}}_{\mathrm{NL}}$ and $b_\phi f^{\text{local}}_{\mathrm{NL}}$ directly from the data for the first time.

III. DATA AND ANALYSIS DETAILS

Our analysis is based on the twelfth data release (DR12) [49] of the Baryon Oscillation Spectroscopic Survey (BOSS). The galaxy clustering data covers two redshift bins with effective centers $z = 0.38, 0.61$, for the Northern and Southern galactic caps, resulting in four independent slices. The BOSS DR12 release contains a total of $\sim 1.2 \times 10^6$ galaxies in a total volume of $6\ (h^{-1}\,\mathrm{Gpc})^3$. From each data chunk, we extract the redshift-space power spectrum multipole moments P_ℓ ($\ell = 0, 2, 4$), the real space power spectrum proxy Q_0 [69], the redshift-space bispectrum monopoles for triangle configurations within the range of $k_i \in [0.01, 0.08)\ h\mathrm{Mpc}^{-1}$ (a total of 62 bispectrum data points per data chunk), and the BAO parameters $\alpha_\parallel, \alpha_\perp$ measured from the post-reconstructed power spectrum data using the method of [70]. Both power spectra and bispectra are measured using window-free estimators [25,26], thus we do not need to include the survey window function in our theoretical model.

We use the data cuts[2] $k_{\max} = 0.25\ h\mathrm{Mpc}^{-1}$, $k_{\min} = 0.01\ h\mathrm{Mpc}^{-1}$ for P_ℓ and $k_{\min} = 0.25\ h\mathrm{Mpc}^{-1}$, $k_{\max} = 0.27\ h\mathrm{Mpc}^{-1}$ for Q_0, so that the two statistics are largely independent. We use lower $k_{\max}$ for Q_0 because the two-loop corrections can be non-negligible compared to the PNG contributions for $k_{\max} > 0.3\ h\mathrm{Mpc}^{-1}$. Note that our choice $k_{\min} = 0.01\ h\mathrm{Mpc}^{-1}$ for both the power spectra and

---

[2]Note that we use $k_{\max}$ for P_ℓ that is slightly larger than that adopted in Ref. [71]. This is because the particular choice of the data cut in that paper $k_{\max} = 0.2\ h\mathrm{Mpc}^{-1}$ was based on detecting biases in the cosmological parameter posteriors. However, in contrast to [71], here we fix all cosmological parameters, in which case the fit to $f^{\text{local}}_{\mathrm{NL}}$ is unbiased up to somewhat larger $k_{\max}$. We stress that this choice is not essential for the purposes of our work, as the $f^{\text{local}}_{\mathrm{NL}}$ constraints are dominated by the linear LPNG bias and hence are saturated at large scales.

bispectra is conservative. We remove the first bin in order to limit systematic effects related to stellar contamination and residual radial and atmospheric systematics, as well as integral constraints.[3]

The power spectra and bispectra used in this work are extracted using the window-free estimators [25,26]. The covariances for our total data vector $\{P_0, P_2, P_4, Q_0, B_0,$ $\alpha_\parallel, \alpha_\perp\}$ for each data chunk are extracted from a suite of 2048 MultiDark-Patchy mocks [74], using the standard empirical covariance matrix estimator.[4]

Our full-shape analysis matches the ones of [48,50,52,70]. Unlike these works, we explicitly fix all cosmological parameters to the Planck 2018 baseline best-fit values [7]. This is done because in this work we are interested only in the constraints on $f_{\rm NL}^{\rm local}$ from the BOSS survey. Formally, this corresponds to a combination of the CMB power spectra and BOSS power + bispectrum data. Thus, in our MCMC analysis we only fit $f_{\rm NL}^{\rm local}$ with an infinitely large flat prior, plus the Gaussian EFT nuisance parameters (encompassing biases, stochasticity, and counterterms).

As discussed in Sec. II F, our fiducial analysis fixes the PNG bias coefficients to values predicted by the dark matter halo relations as functions of the corresponding linear bias b_1 for each data chunk. This choice is optional. In principle, we can fit both b_ϕ and $b_{\phi\delta}$ directly from the data, but the current limits on these parameters are not very constraining, as shown in Sec. VI. Therefore, they are fully consistent with the fits from simulations (44), making it reasonable to fix them for the primary purposes of this paper.

Our analysis is based on the publicly available CLASS-PT code [60]. Since we do not vary cosmology in this study, we compute the full one-loop power spectrum corrections including the LPNG terms only once, utilizing the Planck cosmology, and only vary the bias parameters and $f_{\rm NL}^{\rm local}$ in the likelihood. For the Nseries mocks we recompute the relevant templates to match the Nseries fiducial cosmology. We plan to implement the full cosmology-dependent LPNG calculation in a future update of CLASS-PT, using which we will systematically study the sensitivity of the $f_{\rm NL}^{\rm local}$ constraints to uncertainties in cosmological parameters. Our Markov Chain Monte Carlo (MCMC) analysis is run with the MONTEPYTHON code [80] and is based on the previously-used public likelihoods.[5]

---

[3]As shown in Fig. 19 of [72], weight-based approaches to removing large-scale systematics (such as those applied in [73] and herein) produce comparable results to more sophisticated methods on comparatively large scales. For $k \lesssim 0.01\ h{\rm Mpc}^{-1}$, the differences between different approaches become significant (and the systematics become larger than the statistical errors, if uncorrected), thus these modes are excised from our analysis.

[4]See [75–79] for alternative covariance matrix estimation techniques.

[5]Available at github.com/oliverphilcox/full_shape_likelihoods.

IV. VALIDATION ON MOCKS

As a validation test, we apply our pipeline to Nseries mock catalogs. These catalogs were used by the BOSS collaboration for internal validation tests [49]. The suite consists of 84 semi-independent simulation boxes. The Nseries mocks are designed to reproduce the clustering signal of the high-z NGC BOSS sample. Each box has a similar effective volume and mean effective redshift $z = 0.56$. We fit the mean of 84 Nseries boxes with the covariance of one box, divided by 84. Effectively, this is equivalent to fitting a dataset which is ≈ 40 times larger than the BOSS survey. Just like in the actual BOSS data analysis, we fix all the cosmological parameters (to the true values used in the simulations), and vary only $f_{\rm NL}^{\rm local}$ and nuisance parameters in the fit.

The Nseries mocks were produced for Gaussian initial conditions, which we can recover with our pipeline. Indeed, we find $f_{\rm NL}^{\rm local}$ consistent with zero,

$$f_{\rm NL}^{\rm local} = -4.9 \pm 5.0 \quad \text{at } 68\% \,\text{C.L.,} \qquad (45)$$

with the 1d marginalized posterior shown in Fig. 2. Note that the mean is expected to differ from zero to be different from zero by $(1 - 2)\sigma$ due to random fluctuations. This also gives us an estimate of the theory systematic error, $\Delta f_{\rm NL}^{\rm local}|_{\rm syst} \lesssim 5$, which is less than 0.2σ of the actual BOSS 1d marginalized statistical error (rescaling by the square-root of the volume ratio).

We show the best fit model curves against the Nseries data in Fig. 3. The model with $f_{\rm NL}^{\rm local} = 0$ is visually indistinguishable from the actual best-fit model with $f_{\rm NL}^{\rm local} \approx -5$. Note that in Fig. 3 we plot the mean data vector and divide
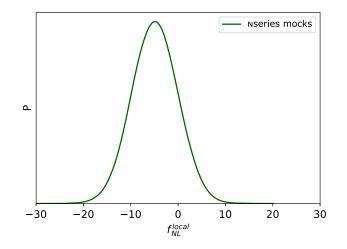

FIG. 2. Marginalized constraint on $f_{\rm NL}^{\rm local}$ from the mean of 84 Nseries simulations, with a total volume approximately 40× larger than that of BOSS. Note that we do *not* rescale the covariance to the BOSS volume, but use that appropriate for the entire Nseries volume, allowing a robust probe of theoretical systematics. Here, we find $f_{\rm NL}^{\rm local} = -4.9 \pm 5.0$ at 68% C.L.
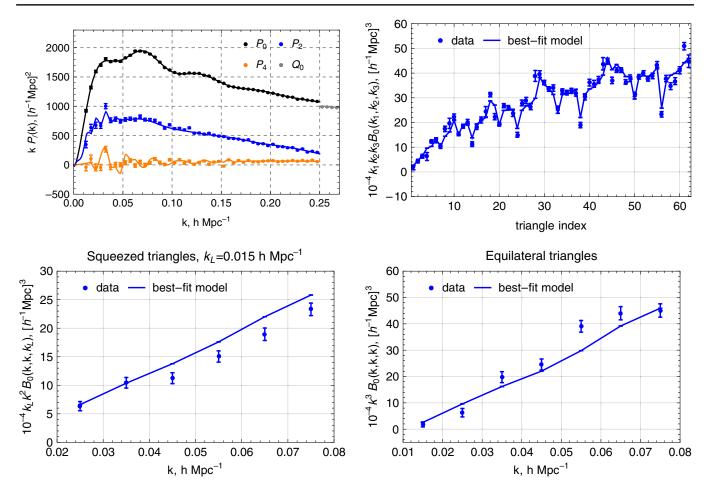
FIG. 3. Mean of Nseries mock power spectra and bispectra from 84 pseudo-independent realizations. Best-fit theoretical models are shown by solid curves. The error bars shown are extracted from the diagonal elements of a covariance matrix corresponding to one mock and divided by $\sqrt{84}$. The nominal size of the errorbars should not be overinterpreted, as the covariance between data points is not negligible. Upper left: power spectra multipoles P_ℓ and Q_0. Note that the jagged behavior of P_2 and P_4 at low wavenumbers are caused by discreteness effects, which we also include in our theory model. Upper right: the bispectrum monopole as a function of the triangle index. Lower left: squeezed configurations of the bispectrum monopole $B_0(k_L, k, k)$ as a function of the bin center k. $k_L < k$ is center of the long modes' bin fixed to $k_L = 0.015\ h\mathrm{Mpc}^{-1}$. Lower right: equilateral configurations $B_0(k, k, k)$.

all error bars by $\sqrt{84}$ as in the actual analysis. At face value, we do not see any strong anomaly in the data. One can notice, however, several data points that deviate from the best-fit curve by more than $(1 - 2)\sigma$. Especially, this is visible in the lower left panel displaying squeezed configurations. We stress, however, that this should not be overinterpreted because of two reasons. First, the 84 Nseries realizations are not completely independent, which may enhance statistical fluctuations in the mean. Second, the data point are significantly correlated. This effect is particularly important for squeezed bispectrum configurations [48,79], which accounts for the apparent disagreement between the theory and the data in the lower left panel. In the end, we see that $f_{\mathrm{NL}}^{\mathrm{local}}$ is recovered without any bias, which proves that our pipeline is adequate for the precision of the BOSS survey.

We stress that the main goal of our validation test is to estimate the bias due to the theory systematic error.

An alternative approach for validation is to fit the mean of the mocks with the covariance that matches the overall volume of the BOSS survey. This test, however, does not allow one to assess the theory bias because the posterior distribution in that case is affected by prior volume effects (arising from the priors necessarily imposed on nuisance parameters), which can be as large as the actual theory bias. This obscures the estimation of theory bias and can lead to wrong conclusions on the validity of the fitting pipeline. For example, the prior volume effects exactly cancel the theory bias on σ_8 for BOSS-like mocks [48,52,81]. Thus, if one fits the mean of the mocks with the covariance matching the BOSS survey volume, one can erroneously conclude that the theory model is valid even for $k_{\mathrm{max}} = 0.3\ h\mathrm{Mpc}^{-1}$, whereas fitting the same data with the actual covariance of the simulation suggests that the theory systematic bias on σ_8 becomes sizable in the analysis of multipoles P_ℓ for $k_{\mathrm{max}} > 0.20\ h\mathrm{Mpc}^{-1}$.

V. RESULTS FOR BOSS

Here, we present the main results from the combined analysis of four BOSS data chunks. We start with the power spectra + BAO data alone, i.e., without the bispectrum. In this case we obtain

$$P_\ell + Q_0 + \text{BAO}: f_{\text{NL}}^{\text{local}} = 9^{+33}_{-35}, \quad (68\%\,\text{C.L.}),$$
$$-57 < f_{\text{NL}}^{\text{local}} < 78, \quad (95\%\,\text{C.L.}). \tag{46}$$

The marginalized posterior distribution is shown in Fig. 4. These results are similar, but somewhat stronger than those obtained previously from BOSS DR9, $-45 < f_{\text{NL}}^{\text{local}} < 195$ (95% C.L.) [18]. This suggests that the constraints in the power spectrum are dominated by the linear scale-dependent bias from large scales. Indeed, repeating our analysis for $k_{\min} = 0.05\,h\text{Mpc}^{-1}$ we find constraints that are worse by a factor of four,

$$k_{\min} = 0.05\,h\text{Mpc}^{-1}: f_{\text{NL}}^{\text{local}} = -120^{+100}_{-140}, \quad (68\%\,\text{C.L.}),$$
$$-353 < f_{\text{NL}}^{\text{local}} < 140, \quad (95\%\,\text{C.L.}). \tag{47}$$

These results are consistent with the expectation that LPNG constraints are dominated by the scale-dependent bias, which is sensitive to the lowest available bin in the survey (see also [23]).

Note that there are important differences between our analysis and that of [18]. That work was based on the monopole power spectrum moment of the BOSS DR9 CMASS sample and had a lower scale cut. In contrast to that, we use all three power spectrum multipole moments plus the
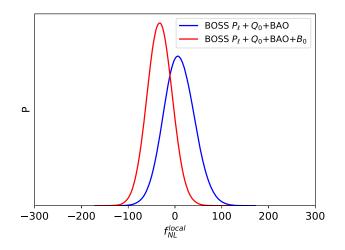

FIG. 4. Marginalized constraints on local-type primordial non-Gaussianity from the BOSS power spectrum (blue) and power spectrum plus bispectrum (red). We find $f_{\text{NL}}^{\text{local}} = 9^{+33}_{-35}$ and -33 ± 28 in the two cases respectively at 68% C.L., with the bispectrum tightening the constraints by $\approx 20\%$. These are the main results of this work.

real space proxy of the complete BOSS DR12 data sample, but impose a conservative scale cut $k_{\min} = 0.01\,h\text{Mpc}^{-1}$, significantly reducing any systematics caused by observational effects, such as galactic foregrounds. Nevertheless, the results of the two analyses are pleasingly consistent.

The addition of the bispectrum monopole shrinks the error bar on $f_{\text{NL}}^{\text{local}}$ by $\simeq 20\%$,

$$P_\ell + Q_0 + \text{BAO} + B_0: f_{\text{NL}}^{\text{local}} = -33 \pm 28, \quad (68\%\,\text{C.L.}),$$
$$-88 < f_{\text{NL}}^{\text{local}} < 23,$$
$$(95\%\,\text{C.L.}), \tag{48}$$

We do not find any evidence for LPNG: the 95% C.L. limits are consistent with zero. The final posterior distribution is presented in Fig. 4. Note that the addition of the bispectrum shifts the mean of the $f_{\text{NL}}^{\text{local}}$ posterior by $\approx 1\sigma$ with respect to the power spectra-only result. This effect in more sizable than the reduction of the marginalized error. Similar trends have been observed in the previous bispectrum analyses [47]. In Appendix C we show that this behavior is quite general for multidimensional likelihoods.

To estimate the dependence of our results on the LPNG priors, we have repeated our analysis assuming the universality relations (43) instead of the more accurate simulation-calibrated fits (44). We found somewhat weaker bounds,

$$\text{Prior (43)}: f_{\text{NL}}^{\text{local}} = -50 \pm 40, \quad (68\%\,\text{C.L.}),$$
$$-130 < f_{\text{NL}}^{\text{local}} < 30 \quad (95\%\,\text{C.L.}). \tag{49}$$

This weakening of the constraints is expected, since the universality relations underpredict the actual values of b_ϕ by $\sim 30\%$ compared to (44) for $b_1 \approx 2$. Note that when the universality bias relations (43) are used, the relative impact of the bispectrum is somewhat stronger: it tightens the constraints by $\simeq 30\%$. The result without the bispectrum in this case is $f_{\text{NL}}^{\text{local}} = 64.7^{+52}_{-60}$.

It is instructive to study where our constraints originate from. To this end we illustrate the effect of the variation of $f_{\text{NL}}^{\text{local}}$ on the galaxy power spectrum and bispectrum monopole, showing the corresponding residuals in Fig. 5. We focus on the NGC z3 data chunk. We first compute the fiducial best-fit theory model with $f_{\text{NL}}^{\text{local}} = 0$. As a second step, the compute models with $f_{\text{NL}}^{\text{local}} = +100$ and $f_{\text{NL}}^{\text{local}} = -100$ while keeping all other parameters fixed. Then in Fig. 5 we plot the difference between the models with $f_{\text{NL}}^{\text{local}} = +100$ and $f_{\text{NL}}^{\text{local}} = -100$, normalized to the fiducial spectra. For the bispectrum monopole, we compute models with $f_{\text{NL}}^{\text{local}} = \pm 300$ in order to make the effect more visible. The shaded gray region corresponds to the BOSS NGCz3 chunk errorbars. The bispectrum residuals are shown as a function of the triangle index which is defined by the bin center (k_1, k_2, k_3). The bin centers here satisfy
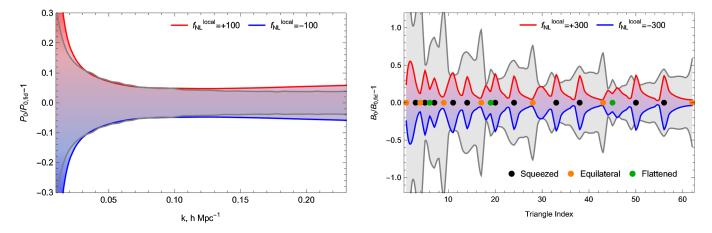
FIG. 5.   Left: residual variations of the galaxy power spectrum monopole model P_0 w.r.t. variations of $f_{\rm NL}^{\rm local}$. These variations have distinctive shape dependence and therefore can be constrained by the data. Right: residual variations of the galaxy bispectrum monopole with respect to variations of $f_{\rm NL}^{\rm local}$. Black, orange and green dots denote the squeezed ($k_3 = 0.015\ h{\rm Mpc}^{-1}$, $k_1, k_2 > k_3$), equilateral ($k_1 = k_2 = k_3$), and flattened ($k_2 = k_3$, $2k_2 = k_1 + 0.015\ h{\rm Mpc}^{-1}$) triangle configurations, respectively.

$k_i \in [0.015, 0.075]\ h{\rm Mpc}^{-1}$, encompassing all wave numbers with $k \in (0.01, 0.08)\ h{\rm Mpc}^{-1}$. We additionally mark the squeezed, equilateral, and flattened triangles with black, orange, and green dots on the x-axis (note that our notation differs somewhat from [50]). The shaded region corresponds to data errors.

Let us first focus on the power spectrum. We observe that the largest deviations take place both on large scales (due to the linear scale-dependent bias), and on short scales due to the one-loop LPNG corrections. This is another indication that the one-loop LPNG corrections should be included in data analysis. Of course, their effect is washed out, to some extent, by marginalization over the standard EFT nuisance parameters, which are important at short scales. Nevertheless, the LPNG nonlinear corrections must to be included for the sake of consistency, and additionally, the degeneracies are greatly reduced in practice by the inclusion of higher-order statistics.

Let us now move on to the bispectrum. We see that the PNG contribution has a very significant configuration-dependence. The LPNG terms peak at the squeezed triangles. This behavior is very different from the typical effect of the standard nonlinear galaxy bias [50], which illustrates that this particular type of non-Gaussianity does not strongly suffer from degeneracy with the unknown galaxy formation details.

Let us compare our results with the $f_{\rm NL}^{\rm local}$ measurements available in the literature. Our limit is a factor of ten worse than the Planck 2018 constraint, $f_{\rm NL}^{\rm local} = -0.9 \pm 5.1$ (68% C.L.) [10]. As we stressed before, our limit is better than the one obtained from BOSS DR9 [18], which is equivalent to $\sigma_{f_{\rm NL}^{\rm local}} \approx 60$. The main reasons for this improvement are new data, the complete theory model for the power spectrum, more accurate priors for LPNG bias parameters, and the large-scale galaxy bispectrum, which is quite sensitive to the scale-dependent bias signal.

Note that our measurement has a precision somewhat worse but comparable with the eBOSS quasars $f_{\rm NL}^{\rm local} = -12 \pm 21$ (68% C.L.) [19,20] (which boast a much longer redshift baseline, and thus a substantially lower $k_{\rm min}$), and with WMAP, $f_{\rm NL}^{\rm local} = 37 \pm 20$ (68% C.L.) [82]. We find comparable results to those from an independent analysis of the BOSS power spectrum and bispectrum (using a partial one-loop theory model for the latter statistic) [30]: $f_{\rm NL}^{\rm local} = -30 \pm 29$, though, as noted above, our analysis differs due to the use of a fully consistent theory model and complete treatment of the survey window, allowing larger-scale information to be robustly included. Finally, our measurements are somewhat better than the ones coming from the UV luminosity function $f_{\rm NL}^{\rm local} = 71^{+426}_{-237}$ (95% C.L.) [83–85], although they include information from scales with $k > 0.3h\ {\rm Mpc}^{-1}$, which we do not consider in our study.

VI. LPNG BIAS PARAMETERS

The galaxy bispectrum allows us to measure $f_{\rm NL}^{\rm local}$ separately from $b_\phi f_{\rm NL}^{\rm local}$. At the power spectrum level this is, essentially impossible, because the constraints are dominated by scale-dependent bias controlled by combination $b_\phi f_{\rm NL}^{\rm local}$ [23]. However, the bispectrum allows us to extract $f_{\rm NL}^{\rm local}$ directly from the $B_{111}^{(s)}$ shape that is generated by the matter clustering and not the LPNG bias. In this section we present the constraints on $b_\phi f_{\rm NL}^{\rm local}$ and $f_{\rm NL}^{\rm local}$ independently. Moreover, we also present constraints on the quadratic scale-dependent bias term $b_{\phi\delta} f_{\rm NL}^{\rm local}$, which shows up in the tree-level galaxy bispectrum with LPNG. We found that $f_{\rm NL}^{\rm local}$ can be quite large in our chains if b_ϕ and $b_{\phi\delta}$ are not fixed, and therefore we have included the $(f_{\rm NL}^{\rm local})^2$ corrections to the tree-level galaxy bispectrum. For these pieces, we keep the additional b_{ϕ^2} bias fixed to the
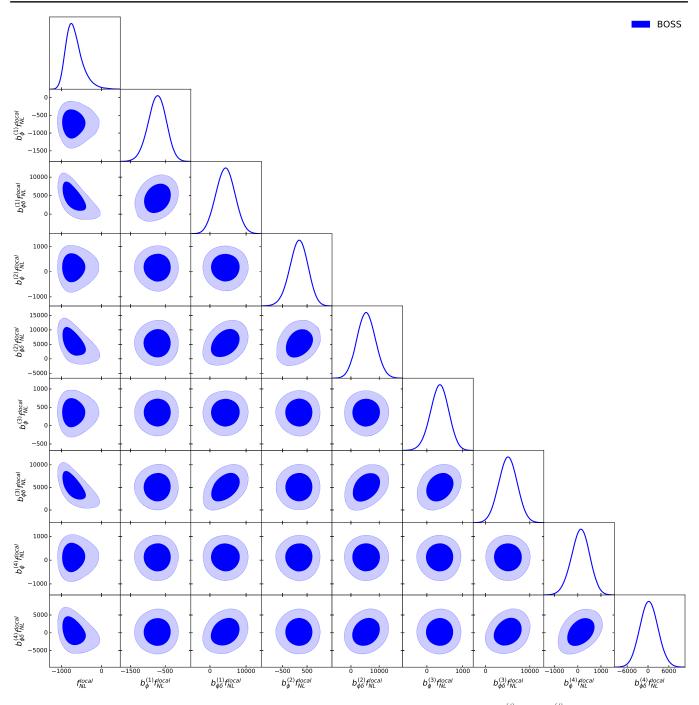
FIG. 6. 1d and 2d marginalized posteriors for $f_{\rm NL}^{\rm local}$ and the normalized LPNG bias parameters $b_\phi^{(i)} f_{\rm NL}^{\rm local}$, $b_{\phi\delta}^{(i)} f_{\rm NL}^{\rm local}$, extracted from the BOSS galaxy power spectra and bispectra data. $i = 1, 2, 3, 4$ corresponds to the NGCz3, SGCz3, NGCz1, and SGCz1 BOSS data slices, respectively.

prediction of the universality relation, as discussed in Appendix A.

We fit $f_{\rm NL}^{\rm local}$ plus parameters $b_\phi f_{\rm NL}^{\rm local}$, $b_{\phi\delta} f_{\rm NL}^{\rm local}$ for each independent data chunk. Our results are displayed in Fig. 6 and Table I. We observe that the BOSS data can constrain the LPNG bias parameter only at the level $\sigma_{b_\phi f_{\rm NL}^{\rm local}} \sim 3 \times 10^2$ and $\sigma_{b_{\phi\delta} f_{\rm NL}^{\rm local}} \sim 3 \times 10^3$. We see that most of the posteriors are compatible with zero values of

corresponding parameters within 95% C.L. However, the parameters $f_{\rm NL}^{\rm local}$, $b_\phi^{(1)} f_{\rm NL}^{\rm local}$, $b_{\phi\delta}^{(3)} f_{\rm NL}^{\rm local}$, overlap with zero only within 99% C.L. of the marginalized posterior. Inspecting the 2d marginalized contours (shown in Fig. 6) suggests that this is a result of degeneracies between $f_{\rm NL}^{\rm local}$ and the LPNG bias parameter combinations. Note that the resulting posteriors are also significantly non-Gaussian, which implies that having nonzero $f_{\rm NL}^{\rm local}$ at 95% C.L. does

TABLE I.   1d marginalized limits for $f_{\mathrm{NL}}^{\mathrm{local}}$ and the normalized LPNG bias parameters $b_\phi^{(i)} f_{\mathrm{NL}}^{\mathrm{local}}$, $b_{\phi\delta}^{(i)} f_{\mathrm{NL}}^{\mathrm{local}}$, extracted from the BOSS galaxy power spectra and bispectra data. $i = 1, 2, 3, 4$ corresponds to the NGCz3, SGCz3, NGCz1, and SGCz1 BOSS data slices, respectively.

Param	Best-fit	Mean $\pm\, \sigma$	95% lower	95% upper
$f_{\mathrm{NL}}^{\mathrm{local}}$	-720	-676^{+150}_{-250}	-1080	-210
$b_\phi^{(1)} f_{\mathrm{NL}}^{\mathrm{local}}$	-878	-740^{+280}_{-250}	-1280	-210
$b_{\phi\delta}^{(1)} f_{\mathrm{NL}}^{\mathrm{local}}$	1900	4300^{+2700}_{-2700}	-950	9500
$b_\phi^{(2)} f_{\mathrm{NL}}^{\mathrm{local}}$	170	160^{+390}_{-360}	-600	900
$b_{\phi\delta}^{(2)} f_{\mathrm{NL}}^{\mathrm{local}}$	5400	5400^{+3200}_{-3400}	-1100	12000
$b_\phi^{(3)} f_{\mathrm{NL}}^{\mathrm{local}}$	180	350^{+270}_{-250}	-170	860
$b_{\phi\delta}^{(3)} f_{\mathrm{NL}}^{\mathrm{local}}$	4400	5000^{+2100}_{-2200}	800	9300
$b_\phi^{(4)} f_{\mathrm{NL}}^{\mathrm{local}}$	26	120^{+420}_{-390}	-700	900
$b_{\phi\delta}^{(4)} f_{\mathrm{NL}}^{\mathrm{local}}$	-22	290^{+2600}_{-2700}	-5000	5700

not actually imply a detection at a significance level equivalent to that of a Gaussian-distributed parameter at 2σ, as evidenced by the lack of detection of LPNG in the fiducial analysis.

Finally, we notice that the posteriors of bias parameters from different data chunks, i.e., $b_\phi^{(1)}, b_\phi^{(2)}$ etc., are randomly scattered by $\lesssim (1-2)\sigma$ around the origin. This behavior is consistent with an expectation of typical shifts due to random statistical fluctuations. This is an additional evidence that our pipeline is not affected by any significant systematic bias.

VII. CONCLUSIONS

We have presented constraints on local primordial non-Gaussianity from the BOSS full-shape galaxy clustering data. The two main novelties of our analysis are (a) we use the full one-loop power spectrum model that includes all necessary nonlinear one-loop corrections generated by LPNG, and (b) we include the consistently analyzed galaxy bispectrum, incorporating a full treatment of all relevant theoretical and observational effects. We have found that the latter improves $f_{\mathrm{NL}}^{\mathrm{local}}$ constraints by 20% compared to the power spectrum analysis. Thus, our paper extends and complements previous works on LPNG from the galaxy clustering data.

There are many ways in which our analysis can be improved. First, the k-range can be expanded, including additional information from both small and large scales. The maximum wave number used in the analysis k_{max} can be significantly enhanced by the addition of the redshift-space galaxy two-loop power spectrum, one-loop bispectrum, as well as the tree-level trispectrum. Partial calculations of these observables already exist in the literature, e.g., [40,86,87], and we plan to incorporate them in our future

analyses. Going beyond perturbative analysis, additional constraints on $f_{\mathrm{NL}}^{\mathrm{local}}$ can be obtained from the nonlinear regime using consistency relations for LSS [88]. They guarantee that the local shape of the bispectrum in the squeezed limit is protected by the equivalence principle and it can be though of as a feature which is very distinct from anything that can be produced by the astrophysical processes. Such feature can be extracted even when the short modes are in the nonlinear regime, marginalizing over the standard nonlinear physics using theoretical error [89,90], similarly to what was done in extracting the BAO feature from the broadband in [70]. In addition, we plan to increase the k-range also on the lower end, by including modes with $k < 0.01h$ Mpc^{-1} that are omitted in the present analysis. This is particularly important in order to enhance constraints from the scale-dependent bias. A simple Fisher forecast indicates that the errors on $f_{\mathrm{NL}}^{\mathrm{local}}$ from BOSS can improve by a factor of two by including all low-k modes. While straightforward from a theoretical point of view, this will require a detailed study of large-scale systematics, such as the integral constraint (both global and radial), foreground stars, atmospheric effects, seeing, and galactic extinction, which can produce large-scale radial and angular distortions, e.g., [72,73]. Such work will be of particular importance as the survey volume increases, and the range of f_{NL} parameters allowed by data tightens. Another important point to keep in mind is that the Gaussian power spectra and bispectra likelihood, which is used in our analysis, is not valid for the lowest k bins and it can skew the constraints on $f_{\mathrm{NL}}^{\mathrm{local}}$. For some recent reflections on how to deal with this problem, see [91].

Second, it would be interesting to study the dependence of the result on the priors on EFT nuisance parameters. Previous works [50,76] have found that marginalization over Gaussian nuisance parameters leads to a very significant degradation of parameter error bars. It is important to understand to what extent this can be avoided with priors on nuisance parameters extracted from high fidelity simulations. We have also shown that our current constraints significantly rely on using universality-like relationships for the LPNG bias parameters $b_\phi, b_{\phi\delta}$. We will study if using relationships is accurate enough for simulated data with injected LPNG. A similar analysis was done in Ref. [23] for the case of real space halo clustering.

Third, one may include redshift-space multipoles of the galaxy bispectrum beyond the monopole moment, which we considered in this work [31]. Fourth, one should perform a systematic sensitivity forecast for future surveys like DESI [92], Euclid [93], and MegaMapper [94]. In particular, just based on the ratio of BOSS and DESI volumes, one may expect improvements by a factor of three, i.e., reaching $\sigma_{f_{\mathrm{NL}}^{\mathrm{local}}} \approx 10$. Some forecasts have already been performed e.g., [95,96], but most of them have been based on simplistic assumptions about the theoretical modeling of the power spectrum and the bispectrum,

and it is rare for forecasts to include both the power spectrum and bispectrum in combination. It will be interesting to see if the inclusion of all necessary nonlinear corrections can impact the conclusions of these works, i.e., to perform a fully consistent forecast similar to [96,97]. Fifth, another important ingredient is a systematic study of the properties of galaxy samples that will be targeted by future surveys, e.g., emission line galaxies admit higher k_{max} and therefore better LPNG measurements can be obtained from this sample [98]. Finally, it would be interesting to extend our analysis to the case of projected statistics, which is motivated by photometric surveys like SPHEREx [11] and the Vera Rubin observatory [99]. This analysis will naturally require including relativistic and full-sky corrections, which can impact constraints on LPNG [100–103], and exploring to what extent the analysis based on correlation functions is optimal and how does it compare to recent results obtained using forward modeling [104].

ACKNOWLEDGMENTS

APPENDIX A: HIGHER ORDER PNG CORRECTIONS TO THE GALAXY BISPECTRUM

In this section we present, for completeness, the bispectrum corrections at $\mathcal{O}(f_{NL}^2)$. To obtain them, we need first include a new bias operator

$$\delta_g^{\text{real space}} \supset \frac{1}{2} f_{NL}^2 b_{\phi^2} \phi^2. \qquad (A1)$$

The full $\mathcal{O}(f_{NL}^2)$ kernel is then given by

$$
\begin{aligned}
B_{NG}^{f_{NL}^2} =\ & Z_1(\mathbf{k}_1)Z_1(\mathbf{k}_2)Z_1(\mathbf{k}_3)b_\phi\left(\frac{1}{Z_1(\mathbf{k}_1)\mathcal{M}(k_1)}+\frac{1}{Z_1(\mathbf{k}_2)\mathcal{M}(k_2)}+\frac{1}{Z_1(\mathbf{k}_3)\mathcal{M}(k_3)}\right)B_{111}(k_1,k_2,k_3) \\
& + \left[b_\phi^2\left(\frac{Z_1(\mathbf{k}_1)}{\mathcal{M}(k_2)}+\frac{Z_1(\mathbf{k}_2)}{\mathcal{M}(k_1)}\right)\frac{(\mathbf{k}_1\cdot\mathbf{k}_2)}{k_1 k_2}\left(\frac{k_1}{k_2\mathcal{M}(k_1)}+\frac{k_2}{k_1\mathcal{M}(k_2)}\right)+f b_\phi^2\mu k\left(\frac{\mu_1}{k_1\mathcal{M}(k_2)}+\frac{\mu_2}{k_2\mathcal{M}(k_1)}\right)\left(\frac{Z_1(\mathbf{k}_1)}{\mathcal{M}(k_2)}+\frac{Z_1(\mathbf{k}_2)}{\mathcal{M}(k_1)}\right) \right. \\
& \left. +2b_\phi^2\frac{Z_2(\mathbf{k}_1,\mathbf{k}_2)}{\mathcal{M}(k_1)\mathcal{M}(k_2)}+b_{\phi\delta}b_\phi\left(\frac{Z_1(\mathbf{k}_1)}{M(k_2)}+\frac{Z_1(\mathbf{k}_2)}{\mathcal{M}(k_1)}\right)\left(\frac{1}{\mathcal{M}(k_1)}+\frac{1}{\mathcal{M}(k_2)}\right)+b_{\phi^2}\frac{Z_1(\mathbf{k}_1)Z_1(\mathbf{k}_2)}{2\mathcal{M}(k_1)\mathcal{M}(k_2)}\right]P_{11}(k_1)P_{11}(k_2). \quad (A2)
\end{aligned}
$$

Finally, the universality relations for the quadratic operators dictate

$$
\begin{aligned}
b_{\phi^2} &= 4\delta_c(b_2^L\delta_c - 2b_1^L), \\
b_{\phi\delta} &= b_\phi + (-b_1^L + \delta_c b_2^L) \\
&= b_\phi - (b_1 - 1) + \delta_c\left[b_2 - \frac{8}{21}(b_1 - 1)\right], \qquad (A3)
\end{aligned}
$$

where $b_1^L \equiv b_1 - 1$ and b_2^L are Lagrangian bias coefficients.

APPENDIX B: ADDITIONAL PLOTS

In this Appendix we present full data vectors and best-fit models from our analysis of the BOSS data. We present a separate plot for each data chunks: NGCz3 in Fig. 7, SGCz3 in Fig. 8, NGCz1 in Fig. 9, SGCz1 in Fig. 10. For all plots we also show best-fit models evaluated with $f_{NL}^{\text{local}} = 0$ (dashed curves). This is noticeable by eye only for the power spectrum monopole, which is consistent with the expectation that most of the constraining power comes from the scale-dependent bias.

APPENDIX C: COMMENT ON THE MEAN VALUE SHIFT IN MULTIDIMENSIONAL LIKELIHOODS

In this section we show that, in the case of multiparameter likelihoods, the size of the shift of a mean value of a certain parameter due to an addition of a new dataset does not have to correlate with the amount of the reduction of the standard deviation. Let us first consider a toy model where we combine two Gaussian likelihoods for a single parameter p. The corresponding individual χ^2 statistics are given by
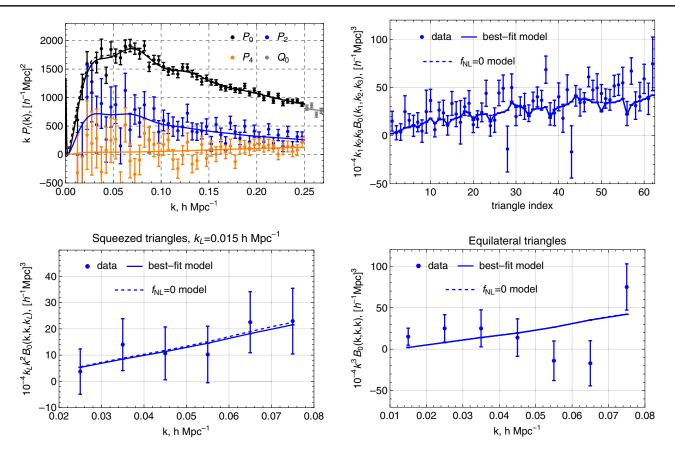
FIG. 7.   Same as Fig. 3, but for the actual BOSS NGC high-z data. Dashed lines show the same best-fit theory model but with fixed $f_{\rm NL}^{\rm local} = 0$.
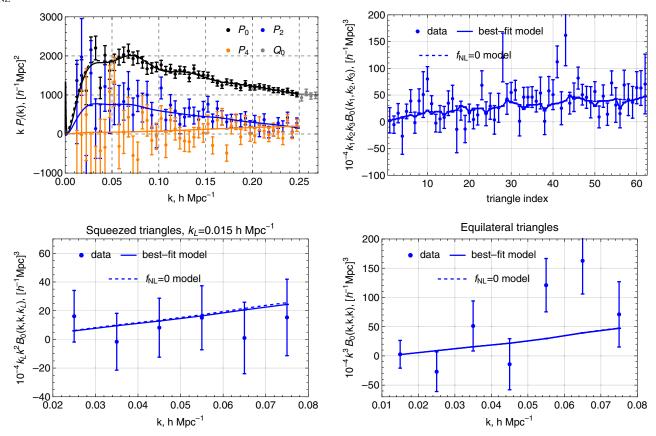

FIG. 8.   Same as Fig. 7, but for the actual BOSS SGC high-z data.
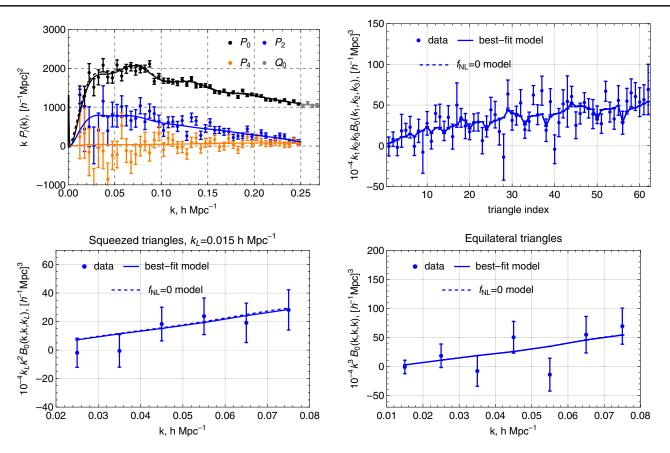
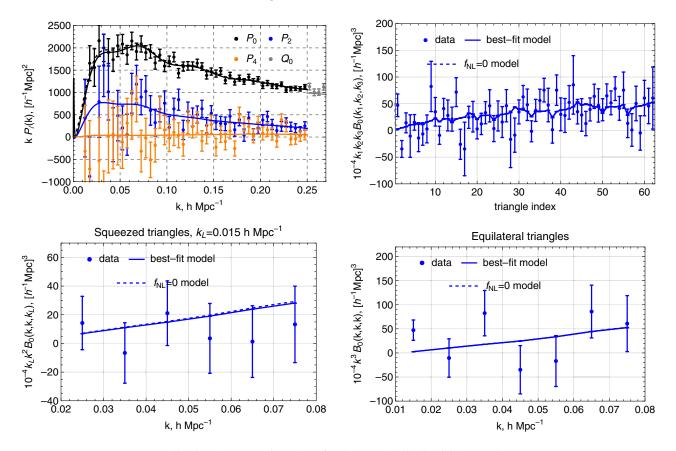FIG. 9. Same as Fig. 7, but for the actual BOSS NGC low-z data.

FIG. 10. Same as Fig. 7, but for the actual BOSS SGC low-z data.

$$\chi^2_{(a)} = \Psi_{(a)}(p - \bar{p}_{(i)})^2, \quad a = 1, 2. \quad \text{(C1)}$$

where Ψ is the 1d precision matrix, $\Psi_{(a)} = \sigma_{(a)}^{-2}$, where $\sigma_{(a)}$ are individual standard deviations and $\bar{p}_{(i)}$ are individual means. The combined likelihood then depends on new χ^2 statistics

$$\chi^2_{\text{new}} = \chi^2_{(1)} + \chi^2_{(2)} = \Psi_{\text{new}}(p - \bar{p}_{\text{new}})^2. \quad \text{(C2)}$$

It is easy to derive the new mean and the new precision matrix (i.e., the standard deviation):

$$\Psi_{\text{new}} = \Psi_{(1)} + \Psi_{(2)}, \quad \bar{p}_{\text{new}} = \frac{\bar{p}_{(1)}\Psi_{(1)} + \bar{p}_{(2)}\Psi_{(2)}}{\Psi_{(1)} + \Psi_{(2)}}. \quad \text{(C3)}$$

Imagine now that the first dataset is more constraining than the second, $\Psi_{(1)} \gg \Psi_{(2)}$, while $\bar{p}_{(1)} \sim \bar{p}_{(2)}$. Then we obtain,

$$\Psi_{\text{new}} = \Psi_{(1)}\left(1 + \frac{\Psi_{(2)}}{\Psi_{(1)}}\right), \quad \bar{p}_{\text{new}} \approx \bar{p}_{(1)} + \frac{\Psi_{(2)}}{\Psi_{(1)}}(\bar{p}_{(2)} - \bar{p}_{(1)}). \quad \text{(C4)}$$

This means that the size of mean shift is correlated with the error bar reduction amount.

Now we generalize our likelihood to the case of N parameters,

$$\chi^2_{(a)} = \Psi^{(a)}_{ij}(p - \bar{p}^{(a)})_i(p - \bar{p}^{(a)})_j, \quad a = 1, 2, \quad j = 1, \ldots, N, \quad \text{(C5)}$$

where we used the Einstein summation notation for dummy indices. Then the χ^2 statistics of the combined likelihood looks like

$$\chi^2_{\text{new}} = \Psi^{\text{new}}_{ij}(p - \bar{p}^{\text{new}})_i(p - \bar{p}^{\text{new}})_j, \quad \text{(C6)}$$

where $\Psi^{\text{new}}_{ij} = \Psi^{(1)}_{ij} + \Psi^{(2)}_{ij}$ and

$$\bar{p}^{\text{new}}_i = [\Psi^{\text{new}}]^{-1}_{il}(\Psi^{(1)}_{lj}\bar{p}^{(1)}_j + \Psi^{(2)}_{lj}\bar{p}^{(2)}_j). \quad \text{(C7)}$$

Imagine that the error bar for a single parameter p_1 reduces only by a small amount after combining datasets 1 and 2. Expanding $\Psi^{\text{new}-1} \approx \Psi^{(1)-1} - \Psi^{(1)-1}\Psi^{(2)}\Psi^{(1)-1}$, we get

$$\sigma_1^2 = [[\Psi^{(1)}]^{-1} - [\Psi^{(1)}]^{-1}\Psi^{(2)}[\Psi^{(1)}]^{-1}]_{11} \simeq \Psi^{(1)}_{11},$$

$$\Rightarrow \frac{[[\Psi^{(1)}]^{-1}\Psi^{(2)}[\Psi^{(1)}]^{-1}]_{11}}{[\Psi^{(1)}]^{-1}_{11}} \ll 1. \quad \text{(C8)}$$

This condition, however, does not imply that the shift of the mean is small. Indeed, at linear order in $\Psi^{(2)}$ we have:

$$\bar{p}^{\text{new}}_1 \approx \bar{p}^{(1)}_1 + [[\Psi^{(1)}]^{-1}\Psi^{(2)}]_{1j}(\bar{p}^{(2)}_j - \bar{p}^{(1)}_j). \quad \text{(C9)}$$

Depending on the structure of the matrix $[\Psi^{(1)}]^{-1}\Psi^{(2)}]_{1j}$, and the vector $(\bar{p}^{(2)}_j - \bar{p}^{(1)}_j)$, one can get a large shift in $\bar{p}^{\text{new}}_1$ even when the standard deviation σ_1^2 is not significantly affected.

Let us give an explicit example of a two dimensional likelihood that reproduces this situation. Consider two Gaussian likelihoods with precision matrices

$$\Psi^{(1)} = \begin{pmatrix} 1 & 3.6 \\ 3.6 & 30 \end{pmatrix}, \quad \Psi^{(2)} = \begin{pmatrix} 0.2 & 0.24 \\ 0.24 & 0.3 \end{pmatrix}, \quad \text{(C10)}$$

and means

$$\bar{p}^{(1)} = (0, 0), \quad \bar{p}^{(2)} = (2, 2), \quad \text{(C11)}$$

so that $(\bar{p}^{(2)}_j - \bar{p}^{(1)}_j) = (2, 2)$. The marginalized errors (σ_1, σ_2) on p_1 and p_2 from these two datasets are $(1.3, 0.24)$ and $(11.2, 9.12)$, respectively. Clearly, the dataset 2 is inferior with respect to the dataset 1. Using our perturbative expression (C8), one can easily obtain that the error bar on p_1 reduces only by $\approx 26\%$,

$$\frac{\Delta\sigma_1^2}{\sigma_1^2} \approx -\frac{[[\Psi^{(1)}]^{-1}\Psi^{(2)}[\Psi^{(1)}]^{-1}]_{11}}{[\Psi^{(1)}]^{-1}_{11}} = -0.26. \quad \text{(C12)}$$

The shift of the mean is, however, quite large,

$$\Delta\bar{p}^{\text{new}}_1 \approx [[\Psi^{(1)}]^{-1}\Psi^{(2)}]_{1j}(\bar{p}^{(2)}_j - \bar{p}^{(1)}_j) = 1.32, \quad \text{(C13)}$$

which is around 1σ in terms of the marginalized error on p_1. In fact, our toy model can be solved exactly,

$$\frac{\Delta\sigma_1^2}{\sigma_1^2} = -0.15, \quad \Delta\bar{p}^{\text{new}}_1 = 1.04, \quad \text{(C14)}$$

which agree with the perturbative estimates (C12) and (C13).

In Fig. 11, we present the individual posteriors for datasets 1,2, and the posterior from their combination. Quantitatively and qualitatively, out toy model reproduces the effect of the bispectrum addition, see Fig. 4.
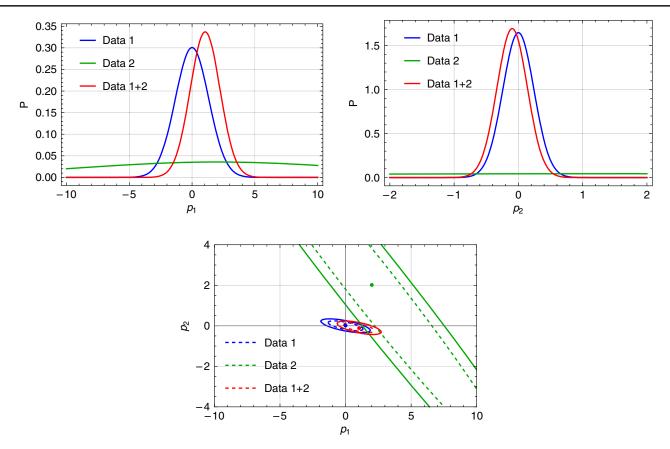
FIG. 11.   1d marginalized distributions (upper panels) and 2d posterior contours (the lower panel) for our toy model of two shifted Gaussian likelihoods. In the lower plot the dashed (solid) curves correspond to 68% (95%) confidence intervals. The optimal value of parameter p_1 shifts noticeable (by $\approx 1\sigma$) after the addition of data 2, while the width of the distribution shrinks only by $\approx 20\%$.

[1] J. M. Maldacena, J. High Energy Phys. 05 (2003) 013.
[2] P. Creminelli and M. Zaldarriaga, J. Cosmol. Astropart. Phys. 10 (2004) 006.
[3] K. Enqvist and M. S. Sloth, Nucl. Phys. **B626**, 395 (2002).
[4] D. H. Lyth and D. Wands, Phys. Lett. B **524**, 5 (2002).
[5] T. Moroi and T. Takahashi, Phys. Lett. B **522**, 215 (2001); **539**, 303(E) (2002).
[6] M. Zaldarriaga, Phys. Rev. D **69**, 043508 (2004).
[7] N. Aghanim *et al.* (Planck Collaboration), Astron. Astrophys. **641**, A6 (2020).
[8] F. Vernizzi and D. Wands, J. Cosmol. Astropart. Phys. 05 (2006) 019.
[9] L. Senatore and M. Zaldarriaga, J. High Energy Phys. 04 (2012) 024.
[10] Y. Akrami *et al.* (Planck Collaboration), Astron. Astrophys. **641**, A9 (2020).
[11] O. Doré *et al.*, arXiv:1412.4872.
[12] S. Ferraro *et al.*, arXiv:1903.09208.
[13] E. Castorina *et al.*, arXiv:2002.05072.
[14] N. Dalal, O. Dore, D. Huterer, and A. Shirokov, Phys. Rev. D **77**, 123514 (2008).

[15] S. Matarrese and L. Verde, Astrophys. J. Lett. **677**, L77 (2008).
[16] A. Slosar, C. Hirata, U. Seljak, S. Ho, and N. Padmanabhan, J. Cosmol. Astropart. Phys. 08 (2008) 031.
[17] J.-Q. Xia, M. Viel, C. Baccigalupi, G. De Zotti, S. Matarrese, and L. Verde, Astrophys. J. Lett. **717**, L17 (2010).
[18] A. J. Ross *et al.*, Mon. Not. R. Astron. Soc. **428**, 1116 (2013).
[19] E. Castorina *et al.*, J. Cosmol. Astropart. Phys. 09 (2019) 010.
[20] E.-M. Mueller *et al.*, arXiv:2106.13725.
[21] R. Scoccimarro, E. Sefusatti, and M. Zaldarriaga, Phys. Rev. D **69**, 103513 (2004).
[22] T. Baldauf, U. Seljak, and L. Senatore, J. Cosmol. Astropart. Phys. 04 (2011) 006.
[23] A. Moradinezhad Dizgah, M. Biagetti, E. Sefusatti, V. Desjacques, and J. Noreña, J. Cosmol. Astropart. Phys. 05 (2021) 015.
[24] A. Barreira, J. Cosmol. Astropart. Phys. 12 (2020) 031.
[25] O. H. E. Philcox, Phys. Rev. D **103**, 103504 (2021).
[26] O. H. E. Philcox, Phys. Rev. D **104**, 123529 (2021).

[27] K. Pardede, F. Rizzo, M. Biagetti, E. Castorina, E. Sefusatti, and P. Monaco, arXiv:2203.04174.

[28] H. Gil-Marín, J. Noreña, L. Verde, W. J. Percival, C. Wagner, M. Manera, and D. P. Schneider, Mon. Not. R. Astron. Soc. **451**, 539 (2015).

[29] H. Gil-Marín, W. J. Percival, L. Verde, J. R. Brownstein, C.-H. Chuang, F.-S. Kitaura, S. A. Rodríguez-Torres, and M. D. Olmstead, Mon. Not. R. Astron. Soc. **465**, 1757 (2017).

[30] G. D'Amico, M. Lewandowski, L. Senatore, and P. Zhang, arXiv:2201.11518.

[31] R. Scoccimarro, H. M. P. Couchman, and J. A. Frieman, Astrophys. J. **517**, 531 (1999).

[32] R. Scoccimarro, Astrophys. J. **544**, 597 (2000).

[33] E. Sefusatti, M. Crocce, S. Pueblas, and R. Scoccimarro, Phys. Rev. D **74**, 023522 (2006).

[34] E. Sefusatti and E. Komatsu, Phys. Rev. D **76**, 083004 (2007).

[35] E. Sefusatti, Phys. Rev. D **80**, 123002 (2009).

[36] T. Baldauf, L. Mercolli, M. Mirbabayi, and E. Pajer, J. Cosmol. Astropart. Phys. 05 (**2015**) 007.

[37] R. E. Angulo, S. Foreman, M. Schmittfull, and L. Senatore, J. Cosmol. Astropart. Phys. 10 (2015) 039.

[38] D. Blas, M. Garny, M. M. Ivanov, and S. Sibiryakov, J. Cosmol. Astropart. Phys. 07 (**2016**) 028.

[39] E. O. Nadler, A. Perko, and L. Senatore, J. Cosmol. Astropart. Phys. 02 (2018) 058.

[40] A. Eggemeier, R. Scoccimarro, and R. E. Smith, Phys. Rev. D **99**, 123514 (2019).

[41] A. Eggemeier, R. Scoccimarro, R. E. Smith, M. Crocce, A. Pezzotta, and A. G. Sánchez, Phys. Rev. D **103**, 123550 (2021).

[42] V. Desjacques, D. Jeong, and F. Schmidt, Phys. Rep. **733**, 1 (2018).

[43] V. Desjacques, D. Jeong, and F. Schmidt, J. Cosmol. Astropart. Phys. 12 (2018) 035.

[44] M. M. Ivanov and S. Sibiryakov, J. Cosmol. Astropart. Phys. 07 (2018) 053.

[45] A. Oddo, E. Sefusatti, C. Porciani, P. Monaco, and A. G. Sánchez, J. Cosmol. Astropart. Phys. 03 (2020) 056.

[46] A. Oddo, F. Rizzo, E. Sefusatti, C. Porciani, and P. Monaco, J. Cosmol. Astropart. Phys. 11 (2021) 038.

[47] M. M. Ivanov, O. H. E. Philcox, T. Nishimichi, M. Simonović, M. Takada, and M. Zaldarriaga, Phys. Rev. D **105**, 063512 (2022).

[48] O. H. E. Philcox and M. M. Ivanov, Phys. Rev. D **105**, 043517 (2022).

[49] S. Alam *et al.* (BOSS Collaboration), Mon. Not. R. Astron. Soc. **470**, 2617 (2017).

[50] G. Cabass, M. M. Ivanov, O. H. E. Philcox, M. Simonović, and M. Zaldarriaga, Phys. Rev. Lett. **129**, 021301 (2022).

[51] A. Perko, L. Senatore, E. Jennings, and R. H. Wechsler, arXiv:1610.09321.

[52] M. M. Ivanov, M. Simonović, and M. Zaldarriaga, J. Cosmol. Astropart. Phys. 05 (**2020**) 042.

[53] G. D'Amico, J. Gleyzes, N. Kokron, D. Markovic, L. Senatore, P. Zhang, F. Beutler, and H. Gil-Marín, J. Cosmol. Astropart. Phys. 05 (**2020**) 005.

[54] M. M. Ivanov, M. Simonović, and M. Zaldarriaga, Phys. Rev. D **101**, 083504 (2020).

[55] T. Nishimichi, G. D'Amico, M. M. Ivanov, L. Senatore, M. Simonović, M. Takada, M. Zaldarriaga, and P. Zhang, Phys. Rev. D **102**, 123541 (2020).

[56] G. Cabass, M. M. Ivanov, M. Lewandowski, M. Mirbabayi, and M. Simonović, arXiv:2203.08232.

[57] A. Taruya, K. Koyama, and T. Matsubara, Phys. Rev. D **78**, 123534 (2008).

[58] V. Assassi, D. Baumann, E. Pajer, Y. Welling, and D. van der Woude, J. Cosmol. Astropart. Phys. 11 (2015) 024.

[59] V. Assassi, D. Baumann, and F. Schmidt, J. Cosmol. Astropart. Phys. 12 (2015) 043.

[60] A. Chudaykin, M. M. Ivanov, O. H. E. Philcox, and M. Simonović, Phys. Rev. D **102**, 063533 (2020).

[61] F. Schmidt, F. Elsner, J. Jasche, N. M. Nguyen, and G. Lavaux, J. Cosmol. Astropart. Phys. 01 (2019) 042.

[62] M. Simonović, T. Baldauf, M. Zaldarriaga, J. J. Carrasco, and J. A. Kollmeier, J. Cosmol. Astropart. Phys. 04 (2018) 030.

[63] D. Blas, M. Garny, M. M. Ivanov, and S. Sibiryakov, J. Cosmol. Astropart. Phys. 07 (**2016**) 052.

[64] A. Vasudevan, M. M. Ivanov, S. Sibiryakov, and J. Lesgourgues, J. Cosmol. Astropart. Phys. 09 (2019) 037.

[65] C. Alcock and B. Paczynski, Nature (London) **281**, 358 (1979).

[66] E. Pajer and M. Zaldarriaga, J. Cosmol. Astropart. Phys. 08 (2013) 037.

[67] A. Barreira, G. Cabass, F. Schmidt, A. Pillepich, and D. Nelson, J. Cosmol. Astropart. Phys. 12 (2020) 013.

[68] A. Barreira, J. Cosmol. Astropart. Phys. 01 (2022) 033.

[69] M. M. Ivanov, O. H. E. Philcox, M. Simonović, M. Zaldarriaga, T. Nishimichi, and M. Takada, Phys. Rev. D **105**, 043531 (2022).

[70] O. H. E. Philcox, M. M. Ivanov, M. Simonović, and M. Zaldarriaga, J. Cosmol. Astropart. Phys. 05 (2020) 032.

[71] O. H. E. Philcox, Z. Slepian, J. Hou, C. Warner, R. N. Cahn, and D. J. Eisenstein, Mon. Not. R. Astron. Soc. **509**, 2457 (2021).

[72] B. Kalus, W. J. Percival, D. J. Bacon, E. M. Mueller, L. Samushia, L. Verde, A. J. Ross, and J. L. Bernal, Mon. Not. R. Astron. Soc. **482**, 453 (2019).

[73] A. J. Ross *et al.* (BOSS Collaboration), Mon. Not. R. Astron. Soc. **464**, 1168 (2017).

[74] F.-S. Kitaura *et al.*, Mon. Not. R. Astron. Soc. **456**, 4156 (2016).

[75] D. Wadekar and R. Scoccimarro, Phys. Rev. D **102**, 123517 (2020).

[76] D. Wadekar, M. M. Ivanov, and R. Scoccimarro, Phys. Rev. D **102**, 123521 (2020).

[77] O. H. E. Philcox, M. M. Ivanov, M. Zaldarriaga, M. Simonovic, and M. Schmittfull, Phys. Rev. D **103**, 043508 (2021).

[78] J. Byun, A. Oddo, C. Porciani, and E. Sefusatti, J. Cosmol. Astropart. Phys. 03 (2021) 105.

[79] M. Biagetti, L. Castiblanco, J. Noreña, and E. Sefusatti, arXiv:2111.05887.

[80] T. Brinckmann and J. Lesgourgues, Phys. Dark Universe **24**, 100260 (2019).

[81] A. Chudaykin, K. Dolgikh, and M. M. Ivanov, Phys. Rev. D **103**, 023507 (2021).

[82] C. L. Bennett et al., Astrophys. J. **208**, 20 (2013).

[83] N. Sabti, J. B. Muñoz, and D. Blas, J. Cosmol. Astropart. Phys. 01 (2021) 010.

[84] N. Sabti, J. B. Muñoz, and D. Blas, Astrophys. J. Lett. **928**, L20 (2022).

[85] N. Sabti, J. B. Muñoz, and D. Blas, Phys. Rev. D **105**, 043518 (2022).

[86] D. Bertolini, K. Schutz, M. P. Solon, and K. M. Zurek, J. Cosmol. Astropart. Phys. 06 (**2016**) 052.

[87] T. Konstandin, R. A. Porto, and H. Rubira, J. Cosmol. Astropart. Phys. 11 (2019) 027.

[88] P. Creminelli, J. Noreña, M. Simonović, and F. Vernizzi, J. Cosmol. Astropart. Phys. 12 (**2013**) 025.

[89] T. Baldauf, M. Mirbabayi, M. Simonović, and M. Zaldarriaga, arXiv:1602.00674.

[90] A. Chudaykin, M. M. Ivanov, and M. Simonović, Phys. Rev. D **103**, 043525 (2021).

[91] M. S. Wang, W. J. Percival, S. Avila, R. Crittenden, and D. Bianchi, Mon. Not. R. Astron. Soc. **486**, 951 (2019).

[92] A. Aghamousa et al. (DESI Collaboration), arXiv:1611.00036.

[93] L. Amendola et al., Living Rev. Relativity **21**, 2 (2018).

[94] D. J. Schlegel et al., arXiv:1907.11171.

[95] D. Karagiannis, A. Lazanu, M. Liguori, A. Raccanelli, N. Bartolo, and L. Verde, Mon. Not. R. Astron. Soc. **478**, 1341 (2018).

[96] N. Sailer, E. Castorina, S. Ferraro, and M. White, J. Cosmol. Astropart. Phys. 12 (**2021**) 049.

[97] A. Chudaykin and M. M. Ivanov, J. Cosmol. Astropart. Phys. 11 (2019) 034.

[98] M. M. Ivanov, Phys. Rev. D **104**, 103514 (2021).

[99] v. Ivezić et al. (LSST Collaboration), Astrophys. J. **873**, 111 (2019).

[100] S. Camera, M. G. Santos, and R. Maartens, Mon. Not. R. Astron. Soc. **448**, 1035 (2015); **467**, 1505(E) (2017).

[101] D. Alonso and P. G. Ferreira, Phys. Rev. D **92**, 063525 (2015).

[102] E. Di Dio, H. Perrier, R. Durrer, G. Marozzi, A. Moradinezhad Dizgah, J. Noreña, and A. Riotto, J. Cosmol. Astropart. Phys. 03 (2017) 006.

[103] E. Castorina and E. di Dio, J. Cosmol. Astropart. Phys. 01 (2022) 061.

[104] A. Andrews, J. Jasche, G. Lavaux, and F. Schmidt, arXiv:2203.08838.

[105] D. Blas, J. Lesgourgues, and T. Tram, J. Cosmol. Astropart. Phys. 07 (2011) 034.

[106] B. Audren, J. Lesgourgues, K. Benabed, and S. Prunet, J. Cosmol. Astropart. Phys. 02 (**2013**) 001.

[107] https://getdist.readthedocs.io/en/latest/.

[108] A. Lewis, arXiv:1910.13970.